DAA/GODDARD

NAGW-685

(NASA-CR-176060) CONTRIBUTIONS TO THE 19TH INTERNATIONAL COSMIC RAY CONFERENCE (California Inst. of Tech.) 50 p
HC A03/MF A01 CSCL 03B

N85-33044
THRU
N85-33059
Unclas
G3/88 24914

CALIFORNIA INSTITUTE OF TECHNOLOGY

PASADENA, CALIFORNIA

STAR
1+15

Contributions to the

19th INTERNATIONAL COSMIC RAY CONFERENCE

LA JOLLA, CALIFORNIA

August 11-23, 1985

Space Radiation Laboratory
California Institute of Technology
Pasadena, California 91125

SRL 85 05-15

TABLE OF CONTENTS

- Continued

TABLE OF CONTENTS (continued)

D1

Cosmic Ray ^{3}He Measurements

R. A. Mewaldt
California Institute of Technology
Pasadena, California 91125 USA

Cosmic ray ^{3}He/^{4}He observations, including a new measurement at ~65 MeV/nucleon from ISEE-3, are compared with interstellar propagation and solar modulation models in an effort to understand the origin of cosmic ray He nuclei.

1. Introduction - The rare isotopes ^{2}H and ^{3}He in cosmic rays are believed to be of secondary origin produced by nuclear interactions of primary ^{1}H and ^{4}He with the interstellar medium. There has recently been renewed interest in these isotopes as a result of indications from high-energy antiproton, positron, and ^{3}He observations that the origin of some primary H and He nuclei may differ from that of heavier cosmic rays. In this paper we report a new observation of low-energy ^{3}He, examine previously reported ^{3}He/^{4}He measurements at both low and high energies, and compare these with calculations of the expected ^{3}He/^{4}He ratio at 1 AU. We find no evidence for an excess of low-energy ^{3}He such as that reported at high energies.

2. Observations - The new observation reported here was made with the Caltech Heavy Isotope Spectrometer Telescope (HIST) on ISEE-3 (now renamed ICE) during quiet-time periods from 8/13/78 to 12/1/78. Figure 1 shows the He isotope distribution from the two highest energy intervals covered by HIST. This data results in a ^{3}He/^{4}He ratio of 0.066±0.016 from 58 to 77 MeV/nucleon. Some of the ^{4}He in this energy interval is "anomalous" cosmic ray (ACR) ^{4}He, which has been corrected for using a decomposition of the ACR and galactic cosmic ray (GCR) fluxes [1], and their time history. The derived correction factor of 1.12±0.06 results in an "observed" GCR ^{3}He/^{4}He ratio of 0.074±0.018.

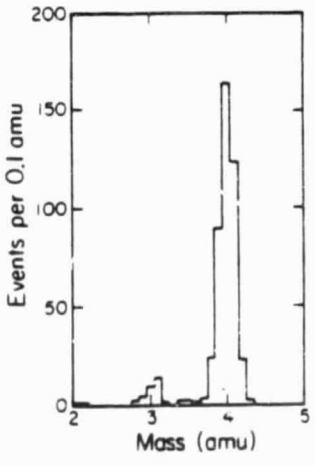

Figure 1: The distribution of quiet-time ^{3}He (48 to 77 MeV/nucleon) and ^{4}He (41 to 67 MeV/nucleon) observed by the Caltech experiment on ISEE-3 during late 1978.

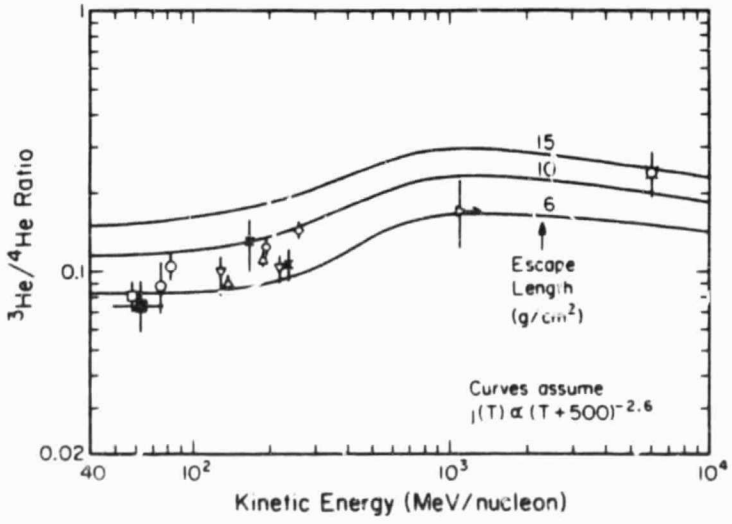

Figure 2: Measured and calculated ^{3}He/^{4}He ratios. Spacecraft observations: ■ This work, 1978; □ Goddard-UNH, 1972 [2]; ○ Chicago, 1973-1974. Balloon data: ▽ Rochester, 1966 [5]; △ UNH, 1972 [6]; × UMd., 1972 [7]; ◇ UNH, 1977 [8]. Geomagnetic method: ▷ Ioffe, 1976 [11]; ⋈ Chicago, 1981 [9,10].

Figure 2 shows our new measurement along with selected other $^3He/^4He$ observations. The spacecraft observations [2,3,4] are from the 1972-1978 solar minimum period and are limited to the 50 to 100 MeV/nucleon interval where contamination by ACR ^4He is minimized. Since the reported observations include ACR ^4He, each has been corrected as described above. Figure 2 also includes observations from ~100 to 300 MeV/nucleon by balloon-borne instruments [5,6,7,8] (here referred to as "the balloon observations"). As discussed in the Appendix, we believe that the observations as reported (and as plotted in Figure 2) have not adequately corrected for ^3He produced in the atmosphere, and a proposed correction (typically ~16%) is therefor applied in subsequent Figures. At >300 MeV/nucleon the only observations use the geomagnetic method, including the recent Jordan and Meyer (J&M) measurement at ~6 GeV/nucleon [9,10], and an earlier result [11]. These experiments also fly on balloons, but are not subject to the same atmospheric corrections.

3. Interpretation of $^3He/^4He$ Observations - To interpret the available $^3He/^4He$ data we use propagation calculations by J. P. Meyer [12], who calculated *interstellar* spectra for ^1H, ^2H, ^3He, and ^4He for a variety of source spectra and mean pathlengths, using the standard "leaky-box" propagation model. The source spectra were of the form $dJ/dT \propto (T + U)^{-2.6}$, where T is kinetic energy per nucleon and $0 \leqslant U \leqslant 938$ MeV/nucleon. We calculated the effects of solar modulation on these spectra using the solar-minimum form of the interplanetary diffusion coefficient from Cummings et al. [13] and numerical solutions of the Fokker-Planck equation including the effects of diffusion, convection, and adiabatic deceleration. Results of these calculations are shown in Figure 2 for source spectra with U=500.

By comparison with the calculations (e.g., Figure 2) each observation determines a "leaky-box" escape-length (λ_e), as shown for U=500 spectra in Figure 3. Note that the spacecraft and (corrected) balloon observations all favor $\lambda_e \simeq 6$ to 7 g/cm^2; only the J&M measurement at ~6 GeV/nucleon indicates $\lambda_e \geqslant 10$ g/cm^2. Table 1 summarizes the mean escape-lengths obtained. Note that the proposed atmospheric correction (see Appendix) lowers the mean escape-length for the balloon observations by ~1.6 to 1.9 g/cm^2 (depending on the spectrum), and generally improves agreement with the spacecraft observations. Table 1 indicates that softer source spectra (e.g., U=200) lead to a somewhat greater λ_e at low energies. This is both a propagation effect (see [12]), and a result of the increased solar modulation required for soft spectra.

4. Discussion - We wish to determine whether the ^3He observations are consistent with the propagation/modulation models derived for heavier nuclei, or whether there is evidence for He nuclei with a separate origin and/or history. For the J&M measurement at ~6 GeV/nucleon we find a pathlength of ~15±6 g/cm^2 (in agreement with their value), independent of the assumed source spectrum. This value is significantly greater than derived from the B/C or other $Z \geqslant 3$ secondary/primary ratios, which imply $\lambda_e \simeq 5.5$ g/cm^2 at ~6 GeV/nucleon [14]. Thus, if the J&M measurement (and its interpretation) is correct, it does imply a high-energy ^3He excess, and a different origin for at least some high-energy He nuclei.

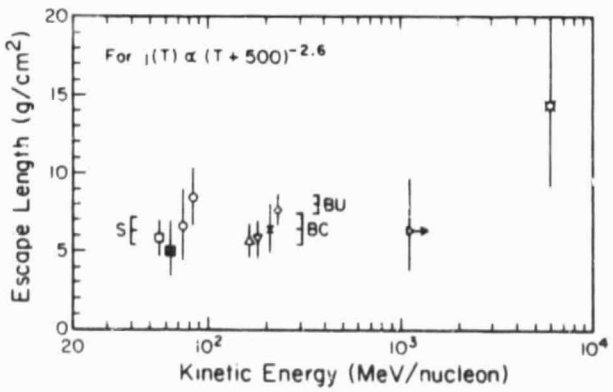

Figure 3: Plot of the escape length determined by the observations in Figure 2. The mean and uncertainty of the spacecraft (S), corrected (BC), and uncorrected (BU) balloon observations are indicated.

Table 1 - Mean Escape-Lengths (in g/cm²)

Source Spectrum	Spacecraft Observations (~ 70 MeV/nuc)	Balloon Observations (~ 200 MeV/nuc) w/o atm. corr.	atm. corr.(1)
$(T+500)^{-2.6}$	6.3±0.9	8.0±0.6	6.4±1.1
$(T+200)^{-2.6}$	8.9±1.0	9.7±0.7	7.8±1.3

(1) Uncertainty includes systematic uncertainty in the magnitude of the atmospheric correction.

At low energies, the required λ_e ranges from ~6 to ~9 g/cm^2 (see Table 1), with the lower value appropriate to U≃500, a spectral form consistent with most studies of the propagation and solar modulation of Z≥3 nuclei (e.g., [15,14]). An escape length of 6 g/cm^2 agrees well with that derived from the B/C ratio at similar energies (see, e.g., [16,14]). We conclude that low-energy observations of ^{3}He/^{4}He are in excellent agreement with the propagation and modulation parameters derived for heavier nuclei.

The above conclusion agrees with most earlier studies of low-energy H and He isotopes that have included both propagation and solar modulation effects (e.g., [17,4,8]), but it is in marked *disagreement* with the recent interpretation of low-energy observations by J&M [9,10]. They suggested that balloon observations at ~100 to 300 MeV/nucleon were consistent with the $\lambda_e \simeq 15$ g/cm^2 escape-length required by their own measurement. After repeating their analysis in detail we conclude that J&M have significantly overestimated the pathlength required by the balloon data, as a result of a combination of factors, and that self-consistent interpretations of the low-energy data imply $\lambda_e(^4\text{He}) \leq 10$ g/cm^2. This conclusion is independent of the magnitude of the proposed atmospheric correction for the balloon data, but it is strengthened by the apparent need for this correction, and also by the spacecraft observations.

Measurements of Z≥3 nuclei imply a energy-dependent escape-length that decreases with energy above several GeV/nucleon. Figure 4 shows the expected ^{3}He/^{4}He ratio for the energy-dependent escape-length ($\lambda_{OP}(E)$) of Ormes and Protheroe [14], for two spectral forms. Both spectra can be seen to be consistent with the low-energy ^{3}He/^{4}He observations and inconsistent with the J&M measurement. Although the U=500 curve falls somewhat above the data, it should be pointed out that $\lambda_{OP}(E) \simeq 9$ g/cm^2 at several hundred MeV/nucleon, which is also greater than required by the B/C ratio. Thus the marginal agreement for U=500 is most likely the result of an inadequacy of the energy dependence of λ_{OP} at low energies.

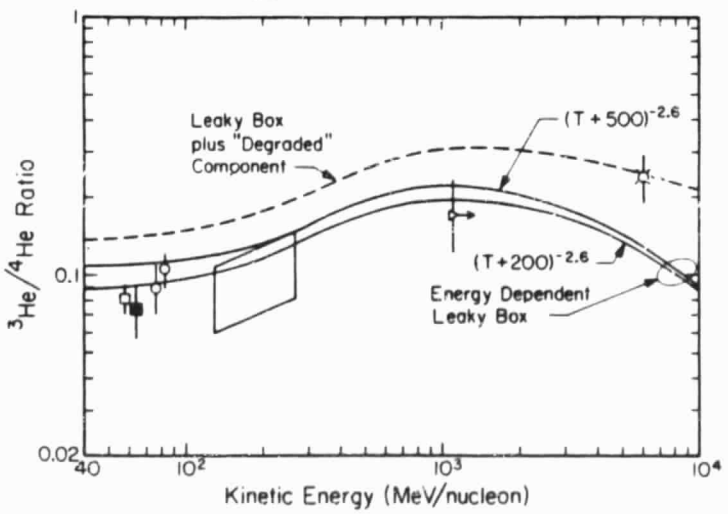

Figure 4: Comparison of the observations with various energy-dependent propagation models (see text). The box indicates the envelope of the corrected balloon observations.

Recent observations of an excess of antiprotons and positrons at high energies have led to several new cosmic ray origin and propagation models in which some nuclei have traversed a great deal of material. Such models also produce an excess of ^{2}H and ^{3}He. As an example, Figure 4 shows the predicted ^{3}He/^{4}He ratio for the model of Cowsik and Gaisser [18], in which a "degraded" component of cosmic rays originates in "thick" sources surrounded by $\sim$50 g/cm^2 of material. While this model is consistent with the J&M observation, it exceeds the observed ^{3}He/^{4}He ratio at low energies. By relaxing the assumption that the "normal" and "thick" sources have the same energy spectra and composition, it might be possible to fit both the high energy data (including the antiproton data) and the low-energy ^{2}H and ^{3}He observations.

Acknowledgements: I thank Dr. J. D. Spalding for performing most of the HIST ^{3}He data analysis, Drs. M. Garcia-Munoz, C. J. Waddington, W. R. Webber, and M. E. Wiedenbeck for discussions of ^{3}He measurements, and Dr. E. C. Stone for helpful comments. This work was supported by NASA under grant NGR 05-002-160 and contracts NAS5-28441 and NAS5-28449.

Appendix - Atmospheric secondaries are an important source of background for balloon-borne ^{2}H and ^{3}He observations. One such contribution, which arises from the breakup of atmospheric N and O nuclei, leads to steeply falling spectra of ^{2}H and ^{3}He that are most significant below $\sim$100 MeV/nucleon (see, e.g., [19,20]). While this source *has* been taken into account in most previous studies, an additional source, due to the breakup of *primary* ^{4}He and heavier nuclei, has generally been ignored. Although we are not aware of appropriate cross section measurements for ^{4}He breaking up into ^{3}He in collisions with CNO, with ^{4}He + p cross sections [12] at $\sim$100 to 300 MeV/nucleon $\sim$0.5 ^{3}He and $\sim$0.4 ^{2}H are produced per inelastic ^{4}He interaction. We might expect ^{4}He + CNO interactions to produce somewhat fewer ^{3}He and more ^{2}H than ^{4}He + p interactions [12], since CNO targets tend to fragment ^{4}He to a greater degree. As an estimate of the "fragmentation parameter" for producing ^{3}He from ^{4}He in interactions with CNO we take $P_{43}=0.25\pm0.15$, in which case a typical ^{3}He/^{4}He ratio of 0.1 at 0 g/cm^2 will increase by $\sim$17% at 3 g/cm^2 due to this process. Using this estimate (see also [21]) we have re-corrected the balloon observations in Figure 2 to the top of the atmosphere. This presently uncertain correction might be measured with observations of ^{3}He/^{4}He vs. atmospheric depth.

References

1. A.C. Cummings, W.R. Webber and E.C. Stone, *Ap. J., 287,* L99, 1984.
2. B.J. Teegarden et al., *Ap. J. 202,* 815, 1975.
3. M. Garcia-Munoz, G.M. Mason and J.A. Simpson, *Ap. J. 202,* 265, 1975.
4. —, *Proc. 14th Int. Cosmic Ray Conf. 1,* 319, 1975.
5. G.D. Badhwar, C.L. Deney, B.R. Dennis and M.F. Kaplon, *Phys. Rev. 196,* 1327, 1967.
6. W.R. Webber and N.J. Schofield, *Proc. 14th Int. Cosmic Ray Conf. 1,* 312, 1975.
7. H.W. Leech and J.J. O'Gallagher, *Ap. J. 221,* 1110, 1978.
8. W.R. Webber and S.M. Yushak, *Ap.J. 275,* 391, 1983.
9. Steven P. Jordan and Peter Meyer, *Phys. Rev. Lett. 53,* 505, 1984.
10. Steven P. Jordan, to be published in *Ap.J.*, 1985.
11. M.G. Jodko, V.K. Karakadko and V.A. Romanov, *Proc. 15th Int. Cosmic Ray Conf. 1,* 292, 1977.
12. J.P. Meyer, thesis, L'Universite Paris, 1974.
13. A.C. Cummings, E.C. Stone and R.E. Vogt, *Proc. 13th Int. Cosmic Ray Conf. 1,* 335, 1973.
14. J.F. Ormes and R.J. Protheroe, *Ap.J. 272,* 756, 1983.
15. M. Garcia-Munoz, G.M. Mason and J.A. Simpson, *Proc. 15th Int. Cosmic Ray Conf. 1,* 301, 1977.
16. M. Garcia-Munoz et al., *Proc. 17th Int. Cosmic Ray Conf. 9,* 195, 1981.
17. R.A. Mewaldt, E.C. Stone and R.E. Vogt *Ap.J. 206,* 616, 1976.
18. R. Cowsik and T.K. Gaisser *Proc. 17th Int. Cosmic Ray Conf. 2,* 218, 1981.
19. P.S. Freier and C.J. Waddington *J. Gepophys. Res. 73,* 4261, 1968.
20. D.J. Hofmann and J.R. Winkler *Planet. Sp. Sci. 15,* 715, 1967.
21. We also assume inelastic mean free paths of 45 and 50 g/cm^2 for ^{4}He and ^{3}He, respectively [8], and that the energy/nucleon and angle of the incident ^{4}He and outgoing ^{3}He are the same.

D2

INITIAL RESULTS FROM THE CALTECH/DSRI BALLOON-BORNE ISOTOPE EXPERIMENT

S. M. Schindler, A. Buffington†, E. C. Christian, J. E. Grove, K. H. Lau & E. C. Stone

California Institute of Technology
Pasadena, California 91125

I. L. Rasmussen & S. Laursen

Danish Space Research Institute, Denmark

ABSTRACT

The Caltech/DSRI balloon-borne High Energy Isotope Spectrometer Telescope (HEIST) was flown successfully from Palestine, Texas on 14 May, 1984. The experiment was designed to measure cosmic ray isotopic abundances from neon through iron, with incident particle energies from ~ 1.5 to 2.2 GeV/nucleon, depending on the element. During ~ 38 hours at float altitude, > 10^5 events were recorded with $Z \geq 6$ and incident energies > 1.5 GeV/nucleon. We present results from the ongoing data analysis associated with both the pre-flight Bevalac calibration and the flight data.

1. Introduction. The experiment described here is a joint undertaking by Caltech and the Danish Space Research Institute. A large-area (geometric factor ~ 0.25 m^2 sr) balloon-borne instrument has been developed to measure cosmic-ray isotopic abundances from neon through iron, with incident particle energies from ~ 1.5 to 2.2 GeV/nucleon, depending on the element (1). The experiment was first flown on 14 May, 1984, from Palestine, Texas. Prior to flight, the detector was exposed to beams of carbon, neon, argon, and manganese at the Berkeley Bevalac, with the latter exposure providing the principal calibration for the instrument. Preliminary results associated with the development of mapping techniques and position-determining algorithms are discussed, with application to flight data.

2. Instrument Description. The experiment employs either Cerenkov-ΔE-Cerenkov or Cerenkov-total energy techniques for isotope resolution (see reference 1), depending on whether the incident particle traverses the entire detector, or stops at an intermediate position in the instrument. Figure 1 shows a schematic diagram of the detector. A stack of twelve NaI(Tl) disks (each nominally 2 cm thick, 52 cm diameter; 87.2 gm/cm^2 total thickness) directly measures the energy change ΔE for an incident particle. Two Cerenkov counters (C1 and C2), measure the change in Lorentz factor, $\Delta\gamma = \gamma_1 - \gamma_2$, for the event. For a stopping particle $\gamma_2 = 1.0$. Mass M is obtained from:

$$M = \Delta E / \Delta\gamma$$

Each disk making up the stack is viewed by six individually digitized photomultiplier tubes (PMT). This permits not only a measurement of the energy deposition per layer, but through intercomparison of the six PMT responses, yields the particle's position in that layer (2,4). Because of the large amount of material

† Present address: Univ. of California, San Diego; CASS C-011, La Jolla, CA 92093

necessary to slow down the high-energy nuclei, typically 85% of the incident particles meeting the trigger requirements will undergo charge-changing fragmentation reactions in the detector. For the NaI stack, these events are removed through a comparison of the individual layer responses. Plastic scintillators (S1 and S2), define the geometry factor, and provide additional rejection against events fragmenting within the Cerenkov counters.

The top Cerenkov counter consists of a mosaic of 48 aerogel radiators of refractive index n ~ 1.1, while the bottom counter employs a combination of teflon (n = 1.34) and Pilot 425 (n = 1.49). Results associated with the ^{55}Mn Bevalac calibration of the aerogel counter have been presented previously (3).

In its flight configuration, the detector and associated electronics are mounted in an insulated pressure vessel. An on-board evaporative cooling system is employed to maintain constant detector temperature, minimizing the need for thermal corrections in the data. Along with housekeeping information, the 108 digitized PMT outputs are recorded on-board using two video recorders, and are also transmitted to the ground through a telemetry link for real-time analysis.

3. Flight Details. The experiment was flown from Palestine, Texas on 14 May, 1984, using a 17.2 x 10^6 ft^3 Winzen balloon. The instrument maintained float altitude for ~ 38 hours, at a typical atmospheric depth of ~ 5.5 gm/cm^2. During the flight, the geomagnetic cutoff ranged from ~ 4.5 to 5.5 GV. The experiment was recovered with minimal damage to the instrument.

For the flight, ~ 4.25 x 10^5 events were recorded, which included > 10^5 events with $Z \geq 6$ and kinetic energy > 1.5 GeV/nucleon. While only a fraction of the events will be usable for isotope analysis, the remainder are being employed for in-flight mapping of the detector, gain balancing, and stability checks.

Analysis of the flight data has shown that with minor exceptions, all systems performed as designed. The evaporative cooler maintained a constant detector temperature of 25.0 ± 0.5°C for the majority of the flight, with a gradient across the NaI stack of ≤ 0.2°C. Examination of threshold settings and detector gains and offsets, have indicated an overall average stability for the flight of better than 1%.

4. Data Analysis. One innovation in this experiment is that the NaI stack provides both trajectory and energy loss information for an incident particle. However, this requires that the response of the individual disks making up the stack be accurately mapped. Previous analysis results have been presented based on the November, 1982 Bevalac calibration, which employed a beam of ^{55}Mn ions, at 1.75 GeV/nucleon (4). Those results were based on analysis of data from two central regions of the instrument. Our primary analysis objective has been to use the ^{55}Mn calibration data to generate full-disk response maps of each PMT viewing each stack layer, and to obtain full-disk maps of the response ratios with various PMT combinations for position determination.

The response maps for each PMT are generated using an overlay of 1 cm bins on each NaI disk. Typically, the response of a single PMT varies by a factor of 5 to 7 across the disk. The current mapping technique uses calibration data to assign an average response to the center of each bin. For each event, a multi-point interpolation process is employed to obtain correction factors from the maps, with the final response generated from a weighted average over all six PMT's viewing the disk.

Figure 2 shows a histogram of the normalized energy loss (response) for layer 1, averaged over the entire disk. The resolution achieved of ~ 2.8% FWHM is only slightly worse than the 2.4% previously reported for central regions of the stack (4). We estimate that Landau fluctuations account for approximately one-half the distribution width. Results for layers 2 and 3 exhibit similar distributions, with a FWHM of ~ 3.0%. Additional refinements in the mapping technique are expected to improve the energy

resolution further.

In addition to generating full-disk response maps, work is progressing on developing position determining algorithms for the disks. Position resolution is obtained from the calibration data, by comparing the measured event position obtained from Bevalac wire-chamber data, and that inferred from algorithms employing ratios of disk PMT responses. The use of PMT response *ratios* effectively removes the energy dependence from the position determination. Currently, six ratio maps are generated for each NaI disk, using a 1 cm spatial grid. The maps employ ratios of opposite sums of two and three adjacent PMT's viewing each disk. Intermediate positions are obtained using an interpolation process. For a given event, the best estimate of particle position is determined from an algorithm which minimizes the difference between the mapped ratios and the measured event ratios.

Figure 3 shows the difference distribution for a single position coordinate (ΔX), as determined from ^{55}Mn calibration data averaged over approximately the central two-thirds area of layer 1. The central portion of the distribution has a FWHM of 4mm, in good agreement with the results previously presented, that were limited to data near the stack axis (4). Similar results are obtained for the orthogonal coordinate ΔY. Combining both position coordinates for layer 1 produces the difference distribution shown in Figure 4, where:

$$\Delta R = (\Delta X^2 + \Delta Y^2)^{1/2}$$

From these results, the rms position resolution for layer 1 is found to be of order 3mm. In extending the analysis to deeper stack layers, the distribution broadens to ~ 4.4mm by layer 5. We consider these results as upper limits to the intrinsic stack resolution, in that contributions from wire-chamber uncertainties and multiple Coulomb scattering have not yet been unfolded from the data.

5. Discussion. While we anticipate further improvement in the analysis results described here, our results for energy resolution are already consistent with the design goals for isotope resolution in the instrument. In particular, if we extrapolate these results to the full 12 layers of the stack for stopping ^{55}Mn, the expected contribution to mass error from uncertainty in ΔE is of order 0.3%. This uncertainty results in an associated mass error for the instrument of ~ 0.1$ amu for Mn at the Bevalac energies, with a correspondingly smaller uncertainty for the lighter elements.

Prior to the detailed analysis of the flight data, the maps and position-determining algorithms developed from the ^{55}Mn Bevalac exposure must be extended to the remaining stack layers. Concurrent with this effort, we are optimizing techniques for trajectory determination, and extending the position-determining algorithms to the outer edges of the disks.

6. Acknowledgements. This work was partially supported by NASA, under grant NGR 05-006-160.

References.

1. Buffington, A., Lau, K., Laursen, S., Rasmussen, I. L., Schindler, S. M., and Stone, E. C., "Proc. 18th International Conference, Bangalore, 2, 49-52, 1983

2. Buffington, A., Lau, K., and Schindler, S. M., "Proc. 17th International Cosmic Ray Conference", Paris, 8, 117-120, 1981.

3. Rasmussen, I. L., Laursen, S., Buffington, A., and Schindler, S. M., "Proc. 18th International Cosmic Ray Conference, Bangalore", 8, 77-80, 1983.

4. Schindler, S. M., Buffington, A., Lau, K., and Rasmussen, I. L., "Proc. 18th international Cosmic Ray Conference, Bangalore", 8, 73-76, 1983.

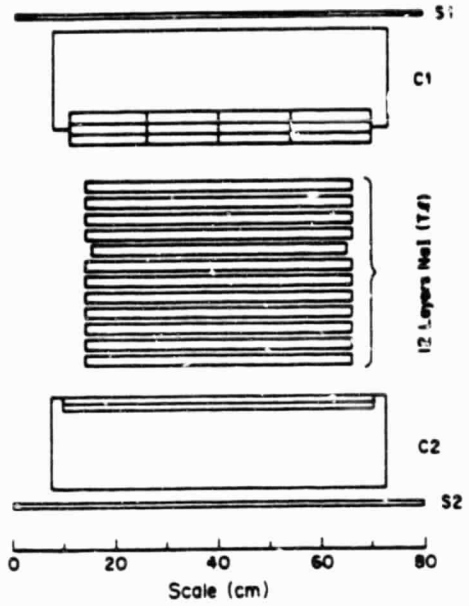

Fig. 1. Schematic diagram of the detector.

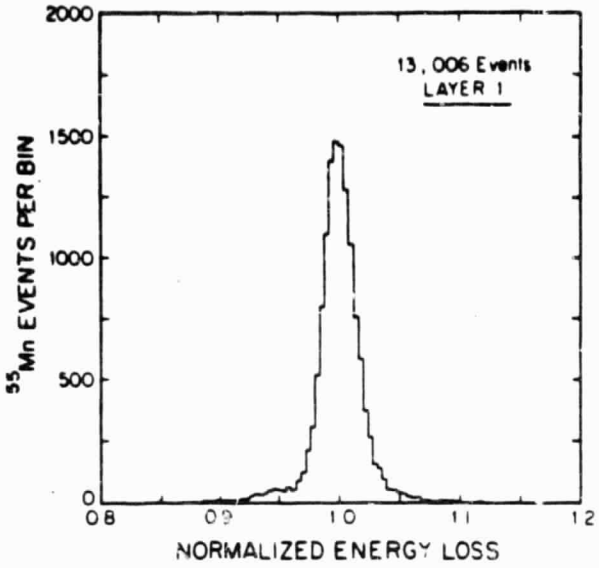

Fig. 2. Layer 1 response distribution for ^{55}Mn, averaged over the full NaI disk.

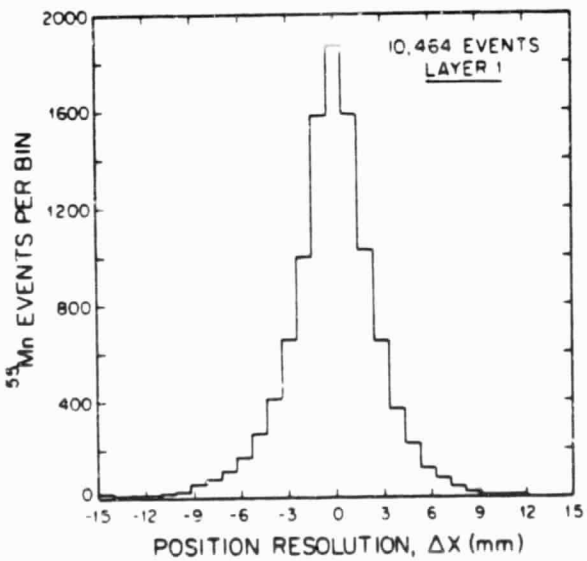

Fig. 3. Difference distribution between a single Bevalac wire-chamber coordinate, and that obtained from layer 1 NaI response ratios, averaged over the central two-thirds area of the disk, for ^{55}Mn ions.

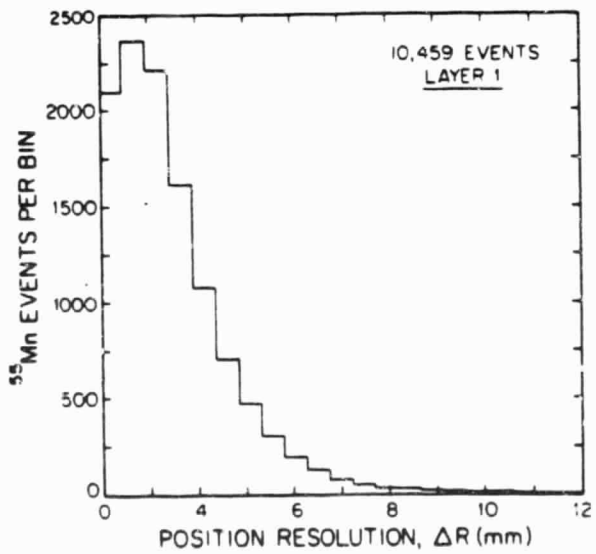

Fig. 4. Difference distribution between Bevalac wire-chamber positions, and those obtained from layer 1 NaI response ratios, averaged over the central two-thirds area of the disk, for ^{55}Mn ions.

Measurements of Fe and Ar Fragmentation Cross Sections

K. H. Lau, R. A. Mewaldt, and E. C. Stone
California Institute of Technology
Pasadena, California 91125 USA

Measurements are reported of the yields of individual isotopes of Cr to Co (Z = 24 to 27) resulting from the fragmentation of ^{56}Fe, and the isotopes of Mg to K (Z = 12 to 19) resulting from the fragmentation of ^{40}Ar.

1. Introduction - Recent advances in the resolution and collecting power of cosmic ray instrumentation, have led to dramatic improvements in the precision of cosmic ray composition measurements, both elemental and isotopic. The interpretation of these measurements is presently limited by uncertainties in the fragmentation cross-sections needed to correct for nuclear interactions with the interstellar gas. Cosmic ray propagation codes now rely mainly on semi-empirical cross-section formulae developed by Silberberg and Tsao (S&T), which have a typical uncertainty of ~25% [1].

We report here relative isotope yields from the fragmentation of ~380 MeV/nucleon ^{56}Fe and ~210 MeV/nucleon ^{40}Ar in CH_2 targets, observed during the calibration of two cosmic ray spectrometers at the Lawrence Berkeley Laboratory Bevalac, and compare these with calculated yields based on the S&T cross-section formulae [1]. Preliminary results from the ^{40}Ar study were reported by Lau, Mewaldt, and Wiedenbeck (LMW) [2].

2. Experimental Setup - The experimental data were obtained during Bevalac runs in April, 1978 (^{56}Fe) and April, 1981 (^{40}Ar). A description of the experimental setup for the ^{40}Ar calibration is given in reference [2]; with additional details in [3]. The setup for the ^{56}Fe run was essentially identical except that the fragmentation products were measured during the calibration of the Caltech Heavy Ion Spectrometer Telescope (HIST) [4], launched on ISEE-3. In the ^{56}Fe run a 587 MeV/nucleon beam was incident on a 5.26 g/cm^2 thick CH_2 target, such that the energy of the interactions ranged from ~100 to 580 MeV/nucleon, with a mean interaction energy of ~380 MeV/nucleon. In the ^{40}Ar runs the beam energy was 287 MeV/nucleon, the CH_2 target thickness 4.1 g/cm^2, and the interaction energy ranged from ~70 to 280 MeV/nucleon with a mean of ~210 MeV/nucleon. We estimate that ~70% (90%) of the analysed interactions occurred in the CH_2 target for the Fe (Ar) runs, the balance taking place in other material including Al and air.

As discussed in LMW, because the experimental setup was designed for calibration purposes, absolute cross-sections could not be measured. In particular, the detectors intercepted only those fragments emitted within ~1° of the beam direction. On the other hand, with the excellent mass resolution achieved, *relative* fragmentation yields can be determined, which are adequate for many cosmic-ray studies (see, e.g., [5]).

3. Data Analysis - For the ^{56}Fe data we use the isotope identification techniques developed for HIST flight data (see, e.g., [6]), where we have restricted the analysis to events stopping in the last four detectors. Figure 1 shows examples of the observed mass distributions, along with Gaussian fits to the data. The excellent mass resolution ($\sigma_m \approx 0.25$ amu) permits the isotopes ^{53}Fe, ^{54}Fe, and ^{55}Fe to be resolved in the presence of (much more abundant) ^{56}Fe. The relative isotope fractions that we observe for Cr, Mn, and Fe fragments are given in Table 1.

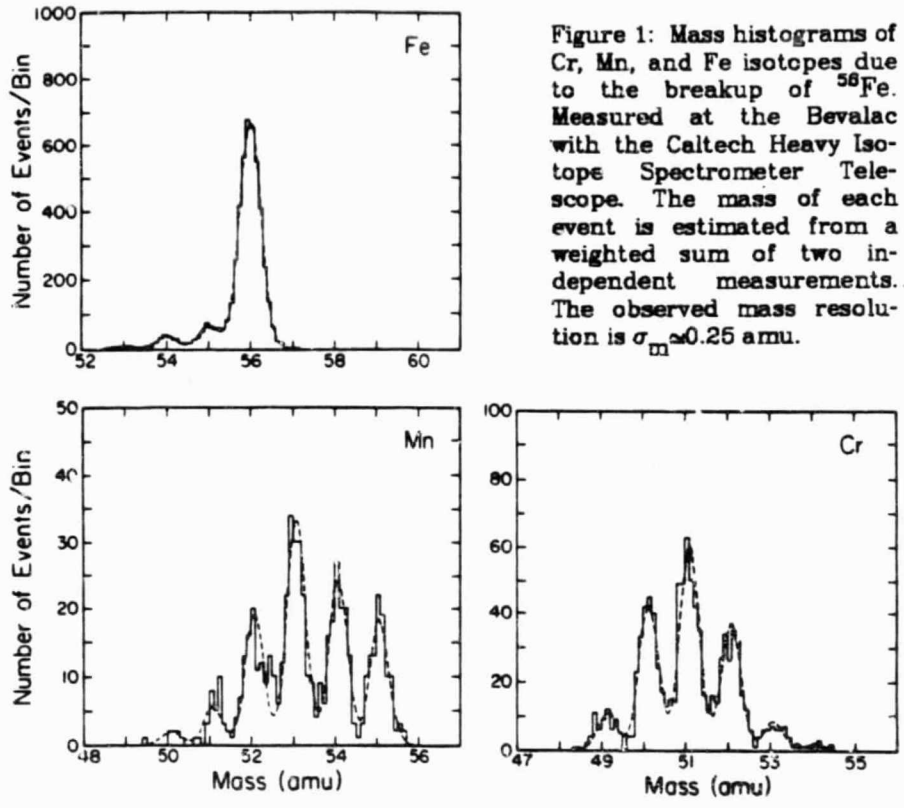

Figure 1: Mass histograms of Cr, Mn, and Fe isotopes due to the breakup of ^{56}Fe. Measured at the Bevalac with the Caltech Heavy Isotope Spectrometer Telescope. The mass of each event is estimated from a weighted sum of two independent measurements. The observed mass resolution is $\sigma_m \approx 0.25$ amu.

The analysis of the ^{40}Ar data set has already been described [2,3]. Table 2 summarizes the fractional yield of isotopes (within each element) for Mg to K fragments ($12 \le Z \le 19$). The $14 \le Z \le 18$ data are essentially the same as those in [2] (with minor differences due to improved statistics and refined corrections), but they are presented in this form for the first time. The Mg and Al data have not been presented before. We find excellent agreement between our isotope fractions and those reported by Viyogi et al. [7], who analyzed the fragmentation of ^{40}Ar in a C target at 213 MeV/nucleon. This suggests that the relative isotope yields do not depend strongly on the target material. Comparing our isotope fractions (Table 2) with those of Viyogi et al. we find no evidence for a mass-dependent bias within an element such as might be introduced by our limited angular coverage.

Table 1 - ^{56}Fe Fragmentation

Isotope	Fraction of Element	
	Observed	Calculated
^{55}Fe	0.669±.010	0.496±.003
^{54}Fe	0.273±.009	0.268±.002
^{53}Fe	0.058±.005	0.236±.002
^{55}Mn	0.215±.007	0.250±.002
^{54}Mn	0.286±.008	0.356±.003
^{53}Mn	0.305±.003	0.220±.002
^{52}Mn	0.146±.006	0.126±.002
^{51}Mn	0.038±.003	0.040±.001
^{50}Mn	0.010±.002	0.008±.001
^{54}Cr	0.026±.003	0.023±.001
^{53}Cr	0.088±.005	0.129±.002
^{52}Cr	0.294±.009	0.375±.002
^{51}Cr	0.315±.009	0.280±.002
^{50}Cr	0.219±.008	0.157±.002
^{49}Cr	0.058±.004	0.036±.001

4. Comparison with Calculated Fragmentation Yields - As described in LMW we have used a Monte Carlo approach developed by M.E. Wiedenbeck to model the experimental setup and calculate the expected yield of each isotope. The calculation takes into account both the energy and target

dependence of the cross-sections [8] for the various materials traversed. Tables 1 and 2 include the calculated isotope fractions for comparison with the observations.

Figure 2 shows a comparison of the measured and calculated isotope yields from ^{56}Fe (normalized to the sum of Cr and Mn). While there is general agreement on the shape of the distributions, there are also significant differences. For example, the calculation predicts Mn/Cr=0.82, while we find Mn/Cr=1.23±0.04, a discrepancy also noted by others [9,10,11] who measured at a variety of energies with C, CH_2, and H targets. Of related astrophysical interest is the result that the radioactive isotope ^{54}Mn fraction is lower than calculated.

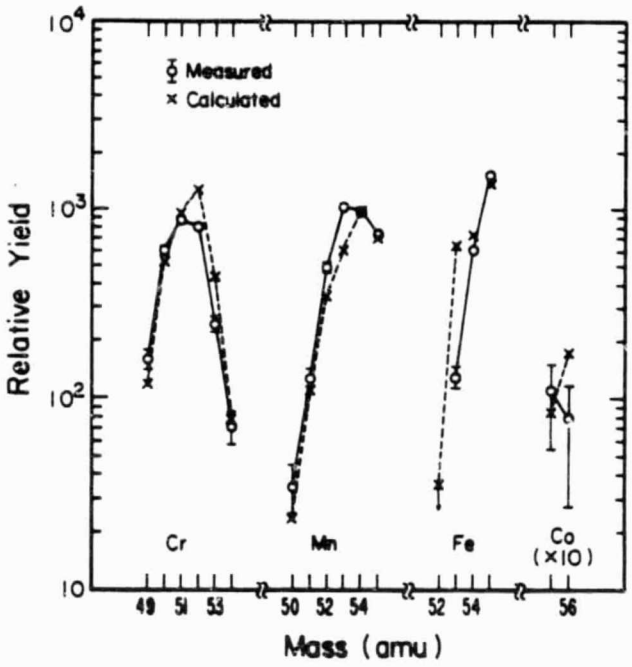

Figure 2: A comparison of measured and calculated yields, normalized to the sum of Mn and Cr.

Table 2 - ^{40}Ar Fragmentation

Isotope	Fraction of Element	
	Observed	Calculated
^{40}K	0.415±.080	0.392±.026
^{39}K	0.585±.080	0.409±.026
^{38}K	<0.03	0.199±.021
^{39}Ar	0.509±.017	0.477±.006
^{38}Ar	0.324±.016	0.357±.006
^{37}Ar	0.125±.011	0.143±.004
^{36}Ar	0.042±.007	0.023±.002
^{39}Cl	0.139±.013	0.130±.004
^{38}Cl	0.146±.012	0.217±.005
^{37}Cl	0.296±.015	0.248±.005
^{36}Cl	0.253±.015	0.273±.005
^{35}Cl	0.115±.011	0.112±.004
^{34}Cl	0.021±.005	0.020±.002
^{38}S	0.009±.003	0.003±.000
^{37}S	0.042±.006	0.027±.001
^{36}S	0.126±.010	0.150±.001
^{35}S	0.218±.012	0.274±.001
^{34}S	0.359±.014	0.377±.002
^{33}S	0.189±.012	0.130±.001
^{32}S	0.057±.007	0.039±.001

Table 2 (continued)

Isotope	Fraction of Element	
	Observed	Calculated
^{36}P	0.027±.006	0.019±.001
^{34}P	0.088±.011	0.088±.001
^{33}P	0.241±.017	0.300±.002
^{32}P	0.341±.019	0.328±.002
^{31}P	0.253±.017	0.211±.002
^{30}P	0.050±.009	0.054±.001
^{32}Si	0.052±.010	0.088±.001
^{31}Si	0.137±.015	0.203±.002
^{30}Si	0.387±.022	0.408±.002
^{29}Si	0.294±.020	0.206±.002
^{28}Si	0.130±.015	0.095±.001
^{30}Al	0.040±.013	0.052±.001
^{29}Al	0.158±.024	0.225±.003
^{28}Al	0.275±.029	0.313±.003
^{27}Al	0.410±.032	0.303±.003
^{26}Al	0.117±.021	0.107±.002
^{27}Mg	0.094±.024	0.145±.002
^{26}Mg	0.306±.038	0.388±.003
^{25}Mg	0.406±.041	0.285±.003
^{24}Mg	0.194±.033	0.182±.003

The two largest discrepancies in either data set are at ^{53}Fe and ^{38}K, both of which are ~6 times less abundant (fraction of element) than calculated. Since both nuclei have 1 less neutron than a "magic number" (n=20-1 for ^{38}K, n=28-1 for ^{53}Fe), their yield may be suppressed if neutron emission is involved. The S&T formulas do not take nuclear shell-structure into account except for a "pairing" correction. Although there are other nuclei with n=19 or n=27 that do not exhibit such a dramatic effect, we suggest that nuclear shell structure should be examined carefully in any attempts to improve semi-empirical cross-sections.

Other significant discrepancies between the observed and calculated fractional yields (e.g., ^{37}Cl, ^{38}Cl, ^{39}Cl, and ^{38}S) involve peripheral reactions, which S&T calculate with special formulae. The agreement for such reactions is better for ^{56}Fe, but these reactions should be less important at the higher energies appropriate to the ^{56}Fe data set.

For both ^{56}Fe and ^{40}Ar fragments the medians of the observed mass distributions are lower than calculated (Figure 2 above and Figure 3 in [2]). There are also differences in the widths of the distributions that are less easily characterized. For both data sets, the ratio of the calculated to measured isotope fractions exhibit rms differences of 25%. Although consistent with the claimed accuracy of the S&T formulae, this demonstrates the need for further cross section measurements if the potential of cosmic ray composition measurements is to be realized.

Acknowledgements: We are grateful to Dr. M. E. Wiedenbeck, who developed the Monte Carlo approach for evaluating the semi-empirical cross-section formulae, for helpful discussions on a number of aspects of this work. Dr. J. D. Spalding was responsible for developing most of the techniques for resolving Fe isotopes in HIST and offered advice on several occasions. We also thank Dr. H. C. Crawford for help with the Bevalac calibrations. This work was supported in part by NASA under grant NGR 05-002-160 and contract NAS5-28449.

References

1. R. Silberberg and C. H. Tsao, *Ap.J. Suppl., 25*, 315, 1973, and *25*, 335, 1973; C.H. Tsao and R. Silberberg, *Proc. 16th Int. Cosmic Ray Conf. 2*, 202, 1979; R. Silberberg, C.H. Tsao, and John R. Letaw, *Composition and Origin of Cosmic Rays*, ed. M.M. Shapiro, Reidel, p. 321, 1983, and references therein.
2. K.H. Lau, R.A. Mewaldt and M.E. Wiedenbeck, *Proc. 18th Int. Cosmic Ray Conf. 9*, 255, 1983.
3. K.H. Lau *Ph.D. Thesis, Caltech, 1985*
4. W.E. Althouse et al., *Geosci. Electronics, GE-16*, 204, 1978.
5. E.C. Stone and M.E. Wiedenbeck *Ap.J., 231*, 95, 1979.
6. R.A. Mewaldt, J.D. Spalding, E.C. Stone and R.E. Vogt, *Ap. J. 235*, L95, 1980.
7. Y.P. Viyogi, et al., *Physical Review Letters 42*, 33, 1978.
8. R. Silberberg and C.H. Tsao, *Proc. 15th Int. Cosmic Ray Conf., 2*, 89, 1977.
9. G.D. Westfall, et al., *Physical Review C, 19*, 1309, 1979.
10. M. Poferl-Kertzman, P.S. Freier and C.J. Waddington, *Proc. 17th Int. Cosmic Ray Conf. 9*, 187, 1981.
11. W.R. Webber and D. Brautigam, *Ap.J. 260*, 894, 1982.

D4

Hexagonal Uniformly Redundant Arrays for Coded-Aperture Imaging

M. H. Finger and T. A. Prince
California Institute of Technology, Pasadena, CA 91125

1. Introduction.

Uniformly redundant arrays are used in coded-aperture imaging, a technique for forming images without mirrors or lenses. This technique is especially important for the high energy x-ray and γ-ray region above 20 keV. In this technique, a mask consisting of opaque (closed) and transparent (open) areas is placed between the photon sources to be imaged and a position sensitive detector or a detector array. Each source casts a shadow pattern of the mask or aperture onto the detector. This shadow pattern may be viewed as an encoded signal for that source direction. If each possible source code is unique, the detected composite of overlapping shadow patterns may be decoded to produce an image of the source distribution.

Figure 1 shows a mask suitable for imaging. This mask consists of an array of open (white) and closed (gray) cells arranged in a periodic pattern. The unit pattern is outlined. The mask in figure 1 is a *uniformly redundant array*[1,2] (URA). URAs have an especially desirable property: the overlap between two source codes is independent of the source directions as long as the sources are sufficiently separated. Except for periodicity, this guarantees a unique decoding of the composite shadow pattern with a maximal immunity to statistical noise.

Figure 1. An HURA of order 79.

To date, most work on URAs has concentrated on those constructed on rectangular lattices. In this paper we focus on URAs constructed on hexagonal lattices, although many of the results are independent of the lattice type.

We will present complete details for the construction of a special class of URAs, the *skew-Hadamard URAs*, which have the following properties:

1) They are nearly half open and half closed.
2) They are antisymmetric (exchanging open and closed cells) upon rotation by 180° except for the central cell and its repetitions.

Some of the skew-Hadamard URAs constructed on a hexagonal lattice have additional symmetries. These special URAs that have a hexagonal unit pattern, and are antisymmetric upon rotation by 60°, we call *hexagonal uniformly redundant arrays* (HURAs). The mask in figure 1 is an HURA.

HURAs are particularly suited to our application, γ-ray imaging in high background situations. In a high background situation the best sensitivity is obtained with a half open and half closed mask. Furthermore, systematic variations of the detector background from position to position can be larger than the variations in detected flux due to sources. With a skew-Hadamard URA a simple rotation turns the mask into a near anti-mask, allowing exact position-by-position background subtraction. Also, the hexagonal symmetry of an HURA is more appropriate for a round position-sensitive detector or a close-packed array of detectors than a rectangular symmetry. This is especially true for shielded detector systems where compactness is at a premium.

2. Mathematical Structure of URAs

A URA is defined within a unit pattern which is repeated periodically. The number of cells in this unit pattern is the order v of the URA. Of these cells, k of them are closed and $v-k$ are open. The uniform redundancy property of URAs involves how frequently a given displacement between closed cells occurs. We will consider a cell within a repetition of the unit pattern as equivalent to the corresponding cell in the unit pattern, and will therefore define the difference between two cell centers as the vector displacement between them, folded back into the unit pattern. For a URA, all possible differences occur a uniform number λ times among the pairs of closed cell centers[2]. This property guarantees the uniform overlap of source codes discussed in the introduction[1,2].

The mathematical structure of a URA is that of an Abelian group difference set[3], which is specified by an Abelian (additive) group G of order v, and a set D of k elements of G with the property that any possible nonzero difference occurs exactly λ times between elements of D. For a URA the group G is the lattice translations modulo the periods of the mask pattern, and the set D contains those translations that take the central cell to a closed cell. The simplest examples of group difference sets are one-dimensional sets known as *cyclic difference sets* defined on the group of integers *mod* v. These play an important role in the construction of many URAs.

URAs in the class consided in this paper, the *skew-Hadamard URAs*, are nearly antisymmetric. That is, for any nonzero element in the group G, either it or its negative but not both, are contained in the difference set D[3]. These skew-Hadamard URAs are a subset of the *Hadamard URAs* which are nearly half open and half closed. Hadamard URAs are characterized by the parameters $v=4n-1$, $k=2n-1$, $\lambda=n-1$ for some integer n.

Johnsen[4] has proven two interesting facts about skew-Hadamard URAs :

1) All skew-Hadamard URAs have a *cyclic* group G, and therefore can be constructed from skew-Hadamard cyclic difference sets.
2) All skew-Hadamard cyclic difference sets are of prime order $v = 3 \ mod \ 4$ and can be generated from the quadratic residues *mod* v .

These facts allow us to present a construction for *all* antisymmetric or skew-Hadamard URAs.

3. Construction of Skew-Hadamard URAs from Quadratic Residues

We now present a simple procedure for generating any skew-Hadamard URA. An example constructed on a hexagonal lattice is shown in figure 2. The procedure consists of the following steps:

1) Choose the lattice on which the URA is to be constructed. The lattice is defined by picking two basis vectors $\overline{e}_0$ and $\overline{e}_1$. For our example we have chosen a hexagonal lattice, which has the basis vectors separated by 60° .
2) Choose as the order of the URA a prime of the form $v = 4n-1$. In our example $v = 23$.
3) Construct the order v skew-Hadamard cyclic difference set from the formula

$$D=\{1^2,2^2,...,(\frac{v-1}{2})^2\} \ mod \ v \qquad (1)$$

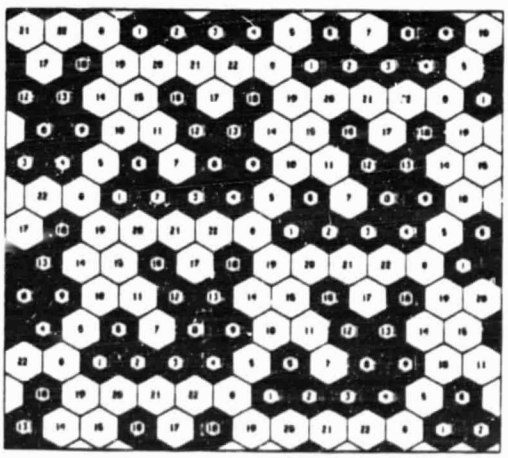

Figure 2. Construction of a skew-Hadamard URA of order 23.

4) Choose an integer r and label all the cells so that the cell centered at $i\overline{e}_0+j\overline{e}_1$ is labeled with

$$l = (i + rj) \ mod \ v \qquad (2)$$

and make all cells with labels in D closed. In our example $r=5$.

The heart of this procedure is the construction of the skew-Hadamard cyclic difference set in step 3. For a proof that this is a difference set see Baumert[3]. Step 4 transfers the difference set properties onto the lattice. This is done through the labeling, which transforms addition *mod* v to vector addition on the lattice modulo the resulting lattice periods.

The freedom available in this procedure rests in the choice of the lattice, the choice of the order v,and the choice of the multiplier r. The lattice type will determine what symmetries can occur. The possible orders form a rather dense set, the first few choices being v=3,7,11,19,23,31,43,47,59,67,71,79, and 83. The multiplier r determines the periods of the URA, and hence the shape of the unit pattern. Many of the v available choices result in URAs that are related by the symmetries of the lattice.

4. Hexagonal Uniformly Redundant Arrays

Of the large number of skew-Hadamard URAs, all of which can be constructed by the procedure in section 3, we wish to pick out those that have a hexagonal unit pattern when constructed on a hexagonal lattice. These we call *hexagonal uniformly redundant arrays* (HURAs)[5]. For an HURA each period when rotated by 60° is again a period. It can be shown from equation (2) that this is only possible if the multiplier r satisfies

$$r^2 = r-1 \quad mod\ v \tag{3}$$

This property has a simple geometric interpretation: a cell labeled l when rotated by 60° will have the label rl *mod* v. This feature, and the properties of quadratic residues modulo a prime, causes this restricted set of URAs to have a rotational antisymmetry upon rotation by 60° as well as 180°.

It can be shown that HURAs exist for order v=3 and any prime order of the form $12n+7$. If HURAs related by symmetry are considered equivalent, then for each of these orders there is a single HURA. The number of available HURAs is still large; figure 3 shows the number of HURAs with order v or less for v up to 10,000. In figures 4 through 8 we show examples of a few moderate order HURAs.

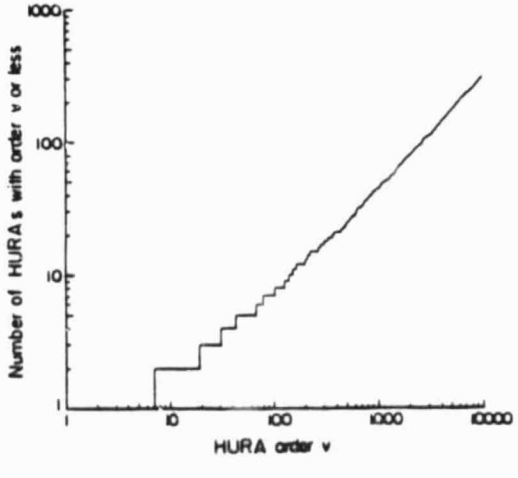

Figure 3. The number of HURAs with a given order or less.

Figure 4. An HURA of order 67.

Figure 5. An HURA of order 139.

Figure 6. An HURA of order 151.

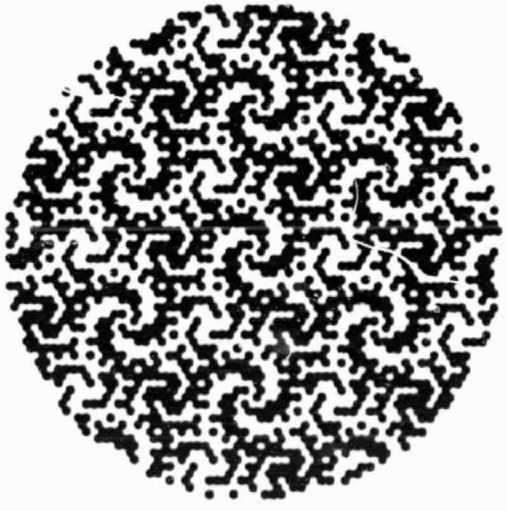

Figure 7. An HURA of order 331.

Figure 8. An HURA of order 619.

While HURAs are mathematically interesting constructs, they also have numerous attractive features for applications in astronomy instrumentation. For instance, the HURA of figure 1 is being implemented as a 115 kg lead coded-aperture mask on a Caltech imaging γ-ray telescope (see OG9.2-2).

5. Acknowledgments

We acknowledge useful discussions with W. R. Cook. This work is supported in part by NASA grant NGR 05-002-160.

References

1) Gunson and Polychronopulos, *Mon. Not. R. Astron. Soc.* **177**,485 (1976)
2) Fenimore and Cannon, *Appl. Opt.*, **17**,337 (1978)
3) Baumert, Cyclic difference sets, *Lecture Notes in Mathematics,No. 182*, Springer-Verlag (1971)
4) Johnsen, *J. Algebra*, **4**,388 (1966) [esp. Corollary 3.4 and Theorem 3.5 restricted to two cycles]
5) Cook et al., *IEEE Trans. Nucl. Sci.*, **NS-31**,771 (1984)

DS

N85-33049

A Balloon-Borne Imaging Gamma-Ray Telescope

W. E. Althouse, W. R. Cook, A. C. Cummings, M. H. Finger, T. A. Prince, S. M. Schindler, C. H. Starr, and E. C. Stone

California Institute of Technology, Pasadena, CA 91125 USA

1. Introduction. This paper describes a balloon-borne coded-aperture γ-ray telescope for galactic and extragalactic astronomy observations. The instrument, called GRIP (Gamma Ray Imaging Payload), is designed for measurements in the energy range from 30 keV to 5 MeV with an angular resolution of 0.6° over a 20° field of view. Distinguishing characteristics of the telescope are a rotating hexagonal coded-aperture mask and a thick NaI scintillation camera. Rotating hexagonal coded-apertures and the development of thick scintillation cameras are discussed in *Cook et al.* [1984 and 1985, referred to as Papers I and II respectively].

2. Instrument Description. The basic elements of GRIP are shown in Figure 1. The telescope consists of a shielded detector system separated by 2.5 m from a lead coded-aperture mask. The primary detector is a position-sensitive scintillator which records the characteristic spatial pattern of photons cast by a γ-ray source through the mask.

The mask is made of lead hexagons 2 cm thick and 2.5 cm across (flat-to-flat), supported by an Al honeycomb sandwich which is transparent at γ-ray energies. The aperture contains 2000

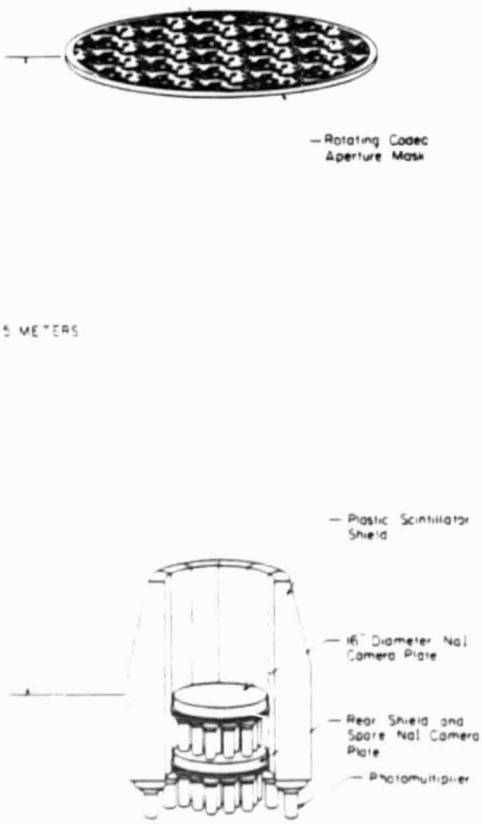

Figure 1.

Table I: **GRIP Balloon Telescope**

Primary Detector	41 cm x 5 cm NaI Anger Camera Position Resolution: < 5 mm rms (0.1 - 5 MeV)
Shield	Back Plate: 5 cm NaI Side: 16 cm plastic scintillator
Mask	Hexagonal URA: 2000 cells (2.5 cm) Rotation Rate: 1 rpm Spacing: 2.5 m from NaI detector Size: 1.2 m diameter x 2 cm (Pb)
Energy Range	0.03 - 5 MeV
Energy Resolution	8.3 keV FWHM @ 50 keV 70 keV FWHM @ 1 MeV
Imaging	Resolution: 0.6° (1070 pixels in 20° FOV) Angular Localization: 3 arc min (10σ source)

hexagonal cells of which half are open and half contain a lead hexagon. The cell pattern (see Figure 2) forms a hexagonal uniformly redundant array (HURA) that is optimal for coded-aperture imaging. HURA's are discussed in more detail in Paper I and in paper OG 9.2-1 in these proceedings.

Continuous mask rotation imposes an additional level of coding on the γ-ray signal. Due to the antisymmetry of the coded-aperture pattern under 60 degree rotation (open and closed cells interchange for all but the central cell) the γ-ray signal at each position on the detector is time-modulated with a 50% duty cycle. This feature allows a complete background subtraction to be performed for each detector position once every 20 seconds assuming a 1 rpm rotation rate. In addition, the continuous rotation permits extension of the field of view to 20 degrees, greatly increasing the number of pixels imaged [Paper I].

Figure 2.
GRIP coded-aperture mask pattern.

The primary detector is a NaI(Tl) camera plate 41 cm in diameter and 5 cm thick manufactured by the Harshaw Chemical Co. The NaI is viewed by nineteen 3 inch Hamamatsu R1307 photomultiplier tubes (PMT's) which are individually pulse height analyzed. The PMT gains are calibrated continuously using pulsed LED's for short term relative gain calibration and an ^{241}Am tagged γ-ray source for long term absolute gain calibration. The ^{241}Am source is situated 1 m above the coded-aperture mask and can be imaged continuously during flight, allowing a thorough checkout of the mask-detector imaging system.

Background suppression is provided by an anti-coincidence shield. On the side are 12 plastic scintillator modules which form a cylinder ~16 cm thick. Each module is viewed by a single 5 inch Hamamatsu R1416 PMT. The lower shield section is a NaI camera plate identical to the primary sensor. Further background suppression is provided by the primary scintillation camera itself. The PMT pulse heights contain information on the depth of the interaction in the crystal. Thus the lower half of the detector can be used as an effective "integral shield" for the reduction of background at low energies [Paper II].

The telescope is mounted on an elevation pointing platform suspended from an azimuthal torquing system. Azimuthal stabilization and orientation are achieved using active magnetometer feedback to the azimuthal torque motor. Elevation orientation is under command control. Two Schonstedt MND-5C-25 magnetometers provide 2-axis aspect information accurate to 1.5 arc minutes. This aspect information is recorded in the telemetry stream and allows correction of the event positions for pointing inaccuracies such as displacement and rotation of the telescope field of view.

For the initial flight of GRIP, we will record all nineteen 12 bit PMT pulse heights for each event. Event rates of up to 5×10^3/s are possible and consequently a data recording system with a 1 Mbit/s data rate is required. We have developed a 1.4 Mb/s recording system with 25 Gbyte capacity using commercial VCR's and audio digitizers. This development is described in paper OG 9.3-11 in these proceedings.

The characteristics of the instrument are summarized in Table I.

3. Instrument Performance.

Position and Energy Resolution: The GRIP scintillation camera has been designed to have ~1 cm FWHM or better position resolution over an energy range from 100 keV to 5 MeV. Figures 3a

and 3b show histograms of γ-ray event positions computed by a maximum likelihood method for beams of photons of 122 keV (^{57}Co) and 662 keV (^{137}Cs) incident on the center of the detector [Paper II]. At the lower photon energy, the 10.5 mm FWHM of the distribution is dominated by photon statistics. At the higher photon energy, both Compton scattering and photon statistics contribute to the 7.0 mm width of the distribution. The effect of Compton scattering is most noticeable in the extended non-Gaussian tails of the distribution.

Although the standard deviation of the distribution of computed event positions increases with energy, the FWHM of the distribution continues to narrow due to an increase in the yield of optical photons per γ-ray event [Paper II]. As a consequence, the point-source angular resolution of the GRIP telescope improves with energy. The primary effect of Compton scattering is a reduction in sensitivity due to a removal of events from the core to the tail of the position distribution.

The energy resolution of the GRIP scintillation camera is comparable to that of single PMT NaI detectors. We have measured a resolution of 7% FWHM at 662 keV.

Imaging: Figures 4a and 4b are laboratory images of 122 keV and 662 keV γ-ray sources taken with the fully configured GRIP telescope. The sources were suspended 10 m from the coded-aperture mask and the imaging algorithms were adjusted to account for the finite distance to the source. The images demonstrate the ability of the telescope to locate and resolve point sources at γ-ray energies.

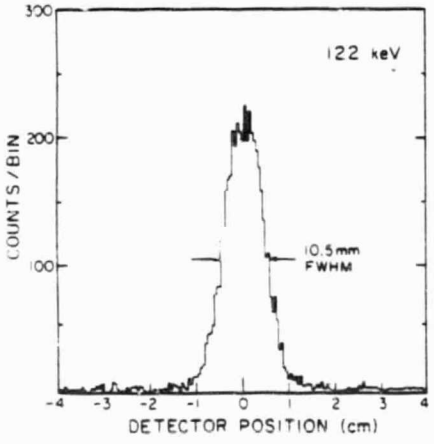

Figure 3a. Histogram of computed event positions showing position resolution at 122 keV.

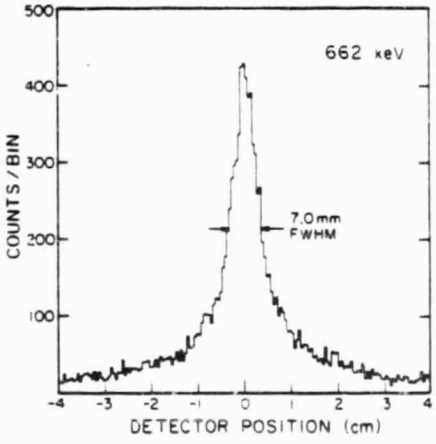

Figure 3b. Histogram showing position resolution at 662 keV.

Effective Area and Sensitivity: The geometrical imaging area of the GRIP scintillation camera is approximately 615 cm^2. This area is determined by the maximum radius (~14 cm) for which good position resolution can be maintained. Additional factors determining the imaging effective area are the point-spread position determination function shown in Figure 3, the full energy detection efficiency, and the mask contrast [Paper I]. Figure 5 shows a plot of imaging effective area versus energy for the GRIP telescope.

The instrument sensitivity depends on the observed background which depends on such factors as flight location, zenith pointing angle, shielding, and instrument mass. We estimate our sensitivity to be approximately 1×10^{-5} ph/cm^2 s kev at 100 keV and 1×10^{-6} ph/cm^2 s kev at 1 MeV for a 3σ 8 hour observation from equatorial latitudes.

4. Flight Plans. The GRIP telescope is scheduled for an initial flight from Palestine, Texas in Fall 1985. Observing targets include the Cygnus region, NGC4151, and the Crab region. Future flights are anticipated from both the northern and southern hemispheres.

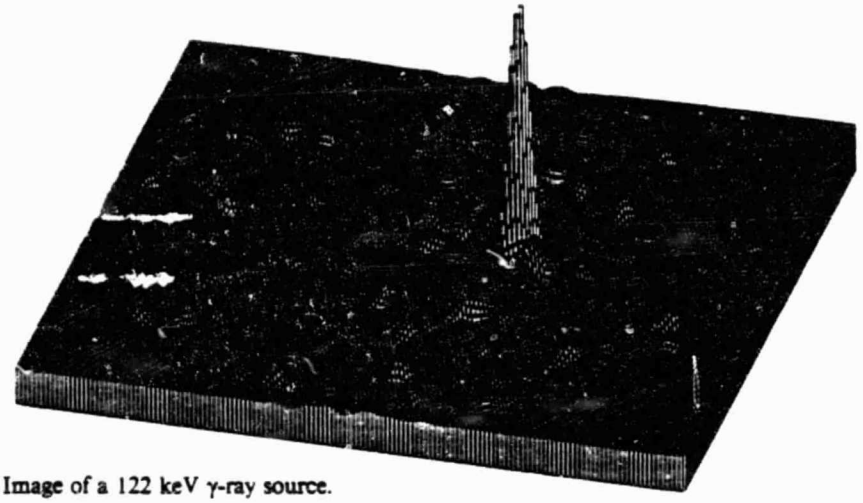

Figure 4a. Image of a 122 keV γ-ray source.

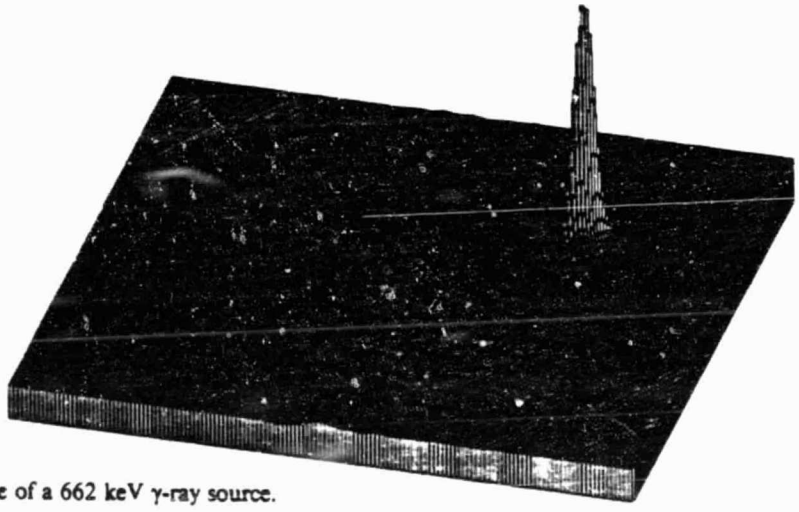

Figure 4b. Image of a 662 keV γ-ray source.

5. Acknowledgments. We thank R. E. Vogt for contributions to this project. This work is supported in part by NASA grant NGR 05-002-160.

6. References

Cook, W.R., Finger, M., Prince, T.A., and Stone E.C., *IEEE Trans. Nucl Sci.*, **NS-31**, 771(1984).

Cook, W.R., Finger, M., and Prince, T.A., *IEEE Trans. Nucl. Sci.*, **NS-32**, 129(1985).

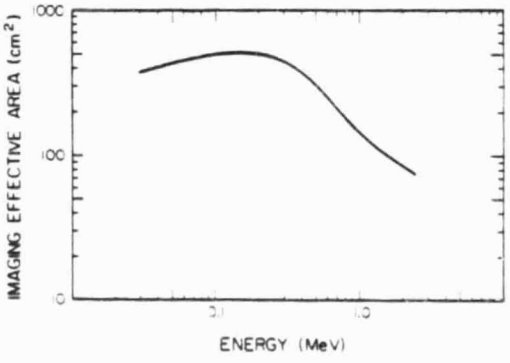

Figure 5. Effective area of the GRIP telescope taking into account position resolution, full-energy detection efficiency, and mask contrast.

Balloon-Borne Video Cassette Recorders For Digital Data Storage

W.E. Althouse and W.R. Cook

California Institute of Technology, Pasadena, CA. 91125, U.S.A.

1. Introduction

A high-speed, high-capacity digital data storage system has been developed for a new balloon-borne γ-ray telescope (see paper OG9.2-2). The system incorporates sophisticated, yet easy to use and economical consumer products: the portable video cassette recorder (VCR) and a relatively newer item - the "digital audio processor". The in-flight recording system employs eight VCRs and will provide a continuous data storage rate of 1.4 megabits/sec throughout a 40 hour balloon flight. Data storage capacity is 25 gigabytes and power consumption is only 10 watts.

2. The Digital Audio Processor

The key to rapid development of a VCR based digital data storage system was the availability of the digital audio processor, a consumer product intended to allow the use of a home VCR as a digital audio tape recorder. A simplified block diagram of such a processor, the Sony PCM-701ES, is shown in Figure 1. In normal stereo recording operation the incoming left and right audio signals are each digitized with 16 bit resolution at a rate of 44 kHz. The digital data are multiplexed onto a single serial line and input to the "record data processor" at a rate of 1.4 megabits/sec. The processor adds error detecting and correcting codes, interleaves the data, and finally generates a video signal in standard NTSC television format suitable for recording on any home VCR. On playback the digital data are unscrambled, corrected for errors, and sent to 16 bit DACs which reconstruct the original audio waveforms. The powerful "cross interleaved" error correction scheme [1,2] virtually eliminates errors due to dropouts on the VCR tape, as is required for noise-free audio reproduction.

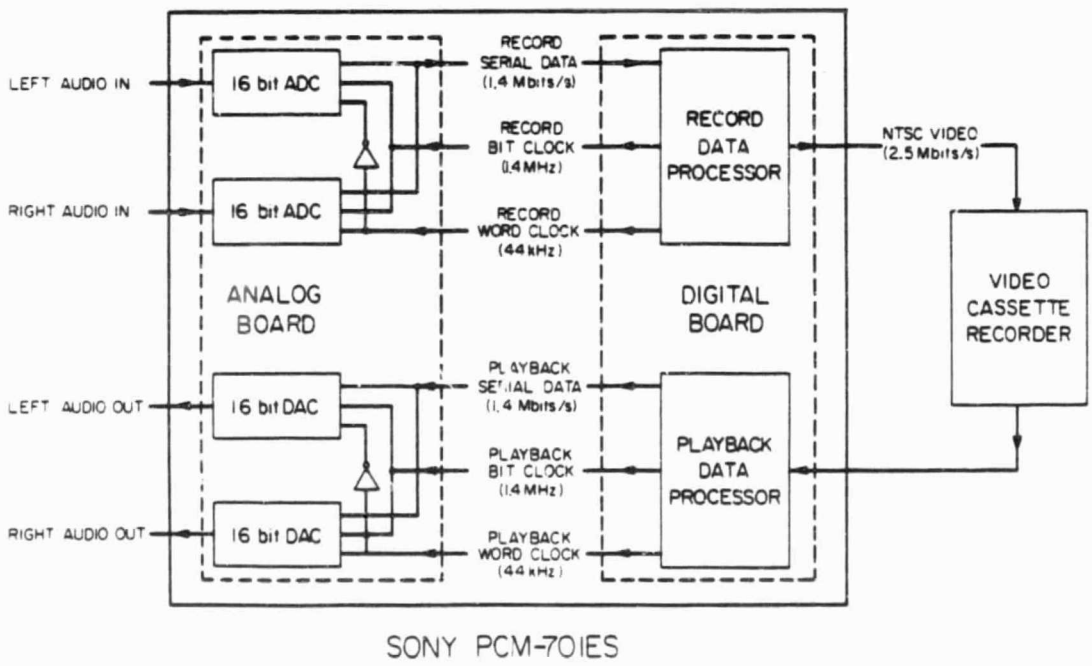

Figure 1. Simplified block diagram of the Sony PCM-701ES Digital Audio Processor.

As shown in Figure 1, the circuitry within the Sony PCM-701ES is conveniently divided into two main printed circuit boards - an analog board and a digital board. For our purpose only the digital board is required. It has been incorporated in our flight recording system (Figure 2) and as part of a record/playback computer peripheral (Figure 3). The digital board is very easy to use. It operates from a single 5 volt supply, is TTL compatible and provides standard 75 ohm video input and output. Power consumption is 3 watts.

The Sony PCM-701ES may be operated in either a 14 or 16 bit mode. In the 16 bit mode the full resolution of the 16 bit ADCs and DACs are used, but fewer error correcting bits are encoded. In the 14 bit mode tape dropouts of up to 32 horizontal television scan lines can be perfectly corrected, while in the 16 bit mode error correction is guaranteed only for dropouts of up to 16 lines [3]. Nonetheless, for the convenience of a simple 16 bit word-aligned format we have used the 16 bit mode. As discused below, the error rate is quite low when high-quality tape is used.

3. Application

In our balloon flight application, γ-ray event data are written into a 2K byte buffer memory while a second buffer memory is read into the PCM-701ES digital board in the format described below. Each buffer can hold 63 events, and buffers are switched synchronously every 11.7 msec, slaved to the PCM-701ES data clock. Thus, ~5400 events per second can be recorded with no deadtime, while the PCM-701ES is supplied with a continuous data stream of 1.4 megabits/sec. The NTSC video signal is fed to eight Sony SL2000 portable VCRs, which are operated sequentially with a capacity of 5 hours recording time for each VCR. Data capacities are summarized in Table I.

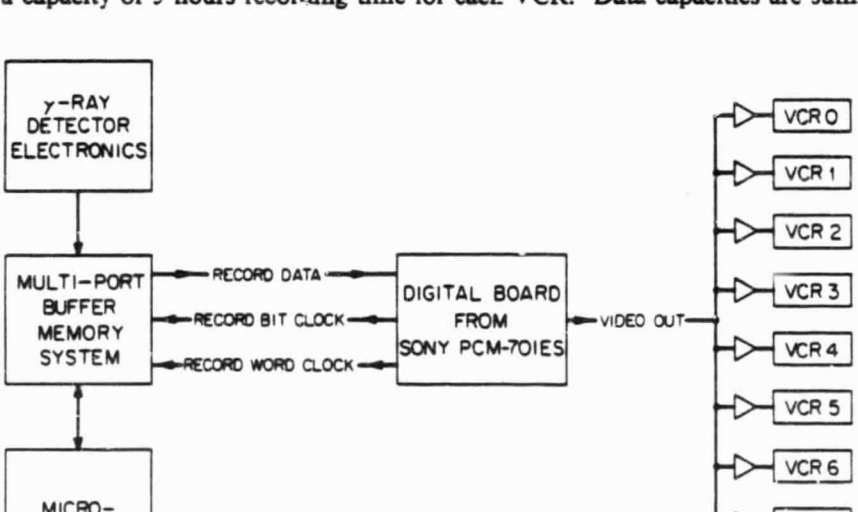

Figure 2. Block diagram illustrating the use of the Sony PCM-701ES digital board in a balloon-borne data recording system.

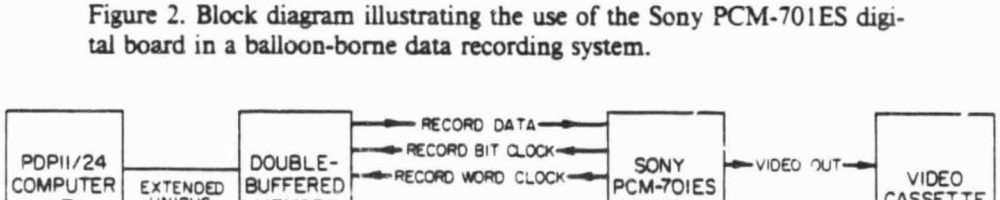

Figure 3. Block diagram showing the Sony PCM-701ES digital board as part of a mass storage computer peripheral.

Table 1. Balloon-Borne γ-ray Telescope Data Storage System	
Data Rate	1.4×10^6 bits/sec 175,000 bytes/sec 5400 events/sec
Recording Time (per tape) (total)	 5 hrs 40 hrs (8 VCRs)
Data Capacity (per tape) (total)	 2.5×10^{10} bits 3.2×10^9 bytes 9.7×10^7 events 2×10^{11} bits 2.5×10^{10} bytes 7.8×10^8 events
Power Consumption Digital board Portable VCR (total)	 3 watts 7 watts 10 watts

We have measured the error rate using Sony L750 Ultra High Grade tape recorded at "βIII" speed on Sony SL2000 portable VCRs. In initial tests approximately 1.5 million 2K byte data blocks were recorded on each of seven video cassettes using seven different VCRs (21 gigabytes total). Each data block contained a 32 bit start code, a 32 bit block count, approximately 1000 psuedo-random 16 bit numbers, a 32 bit stop code and a 16 bit cyclic redundancy check (CRC) code. The tapes were played back on a single VCR and each data block was checked for an accurate start and stop code, CRC error, and sequential block count. Of the 10.5 million blocks checked ~300 were missing (due to "playback muting", where the PCM-701ES simply replaced long stretches of uncorrectable data with a fixed data word), and 19 CRC errors were detected (due to "playback interpolation" where the PCM-701ES replaced isolated uncorrectable data words with the average of adjacent words). The fraction of blocks discarded due to detected errors was $\sim 3 \times 10^{-5}$, a negligible data loss rate for most data acquisition applications. A sample of 600,000 "good" blocks were checked 100% for undetected errors and none were found. Thus the undetected block error rate was less than 2×10^{-6}, acceptable for our present application.

The VCR data systems discussed here were used to record and playback data for the formation of the γ-ray images presented in paper OG9.2-2. In this process 56 megabytes of data were recovered without a single detected error.

This work was supported in part by NASA grant NGR 05-002-160.

4. References

[1] Doi, T.T., Odaka, K., Fukuda, G., Furukawa, S., "Cross Interleave Code for Error Correction of Digital Audio Systems", Audio Engineering Society Preprint, 1979.

[2] Doi, T.T., Tsuchiya, Y., and Iga, A., "On Several Standards for Converting PCM Signals into Video Signals", *J. Audio Eng. Soc.*, **26-9**, pp. 641-649, 1978.

[3] Sony PCM-701ES Operating Instructions, 1983.

D7

ABST ONLY

N85-33051

The Energy Spectrum of Jovian Electrons in Interplanetary Space

S. P. Christon, A. C. Cummings, and E. C. Stone

California Institute of Technology, Pasadena, CA 91125 USA

W. R. Webber

University of New Hampshire, Durham, NH 03824 USA

In this paper we report on the energy spectrum of electrons with energies ~10 to ~180 MeV measured with the electron telescope on the Voyager 1 and 2 spacecraft [*Stone et al.*, 1977] in interplanetary space from 1978 to 1983. The kinetic energy of electrons is determined by double dE/dx measurements from the first two detectors (D_1, D_2) of a stack of eight solid state detectors and by the range of particle penetration into the remaining six detectors (D_3 to D_8) which are interleaved with tungsten absorbers.

From 1978 to 1983 (radial range ~2 to ~12 AU) electrons of jovian origin were clearly observable for electrons stopping in D_3 ($E \gtrsim 4$ MeV) and in D_4 ($E \gtrsim 8$ MeV). For electrons stopping in D_5 ($E \gtrsim 12$ MeV), the jovian flux dominated the galactic electron flux for a period of approximately one year near the encounter with Jupiter [*Christon et al.*, 1985]. Jovian electrons were also observed in D_6 ($E \gtrsim 21$ MeV) but not in D_7 ($E \gtrsim 28$ MeV). A detailed interpretation of the electron variations in all energy channels depends on an accurate subtraction of background induced by energetic protons of a few 100 MeV. This subtraction is facilitated by laboratory calibration results at several energies. Further results on the differential energy spectrum of jovian electrons and limits on the maximum detected energies will be reported.

This work was supported in part by NASA under contract NAS 7-918 and grant NGR 05-002-160.

References.

Christon, S. P., A. C. Cummings, E. C. Stone, and W. R. Webber, *19th Internat. Cosmic-Ray Conf., La Jolla*, paper SH4.7-4, 1985.

Stone, E. C., R. E. Vogt, F. B. McDonald, B. J. Teegarden, J. H. Trainor, J. R. Jokipii, and W. R. Webber, *Space Sci. Rev., 21*, 355, 1977.

D8

N85-33052

Precision Measurements of Solar Energetic Particle Elemental Composition

H. Breneman and E. C. Stone

California Institute of Technology
Pasadena, California 91125 USA

1. Introduction

Using data from the Cosmic Ray Subsystem (CRS) aboard the Voyager 1 and 2 spacecraft (Stone et al. 1977), we have determined solar energetic particle abundances or upper limits for all elements with $3 \leq Z \leq 30$ from a combined set of 10 solar flares during the 1977-1982 time period. Statistically meaningful abundances have been determined for the first time for several rare elements including P, Cl, K, Ti and Mn, while the precision of the mean abundances for the more abundant elements has been improved by typically a factor of ~3 over previously reported values. When compared to solar photospheric spectroscopic abundances, these new SEP abundances more clearly exhibit the step-function dependence on first ionization potential previously reported by Cook et al. (1979, 1984) and Meyer (1981, 1985).

2. Observations

Each CRS includes four Low Energy Telescopes (LET) and two High Energy Telescopes (HET) employing silicon solid-state detectors and covering a combined incident energy range for oxygen of 3.5 - 50 MeV/nucleon. A scatterplot of LET data from the Z = 14 - 20 charge range is shown in Fig. 1. Even relatively rare elements such as Ar and Ca are clearly resolved. For the rarer elements (e.g., P, Cl, K), the abundances were determined by performing maximum-likelihood fits to the rare element peak and its two usually more abundant neighbors. For the most abundant elements (C, N, O, Ne, Na, Mg, Al, Si, S, Ar, Ca, Cr, Fe), the abundances could be determined in each of the flares; these values were averaged to obtain mean abundances using a weighting technique that takes into account both statistical variations and real abundance variations from flare to flare.

3. Results

The average SEP abundances relative to silicon for elements with $3 \leq Z \leq 30$ are listed in Table I. In Fig. 2, these results for the more abundant elements are compared to those obtained by other recent investigations. It can be seen that the new abundances agree well with the previously determined values but have about a factor of three higher precision.

4. Discussion

An ordering by first ionization potential (FIP) of SEP composition relative to "solar system" or photospheric composition has been noted in the past (Hovestadt 1974; Webber 1975; McGuire et al. 1979). In particular, Cook et al. (1979, 1984) found a step-function dependence on FIP, with elements with FIP > 10 eV depleted by a factor of ~5 in SEPs and elements with FIP < 8 eV approximately equally abundant in SEPs and the photosphere. This behavior may be expected on the basis of

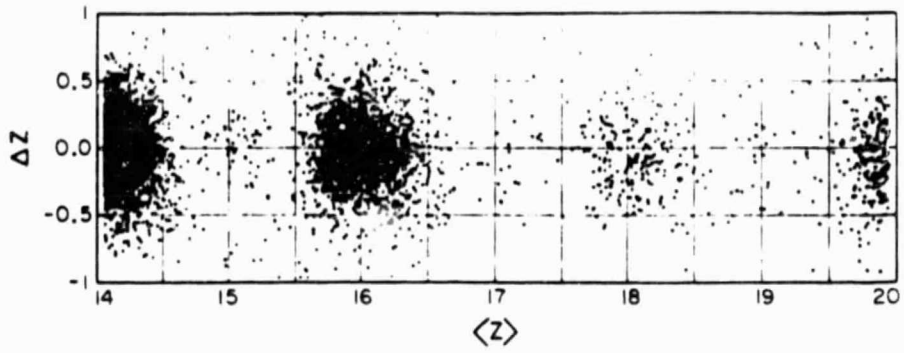

Fig. 1. Scatterplot of SEP data from LET in the Z = 14 - 20 charge range. <Z> is the average, and ΔZ the difference, of two essentially independent charge determinations obtained from the LET data for each analyzed particle.

dynamical ionization models such as that of Geiss and Bochsler (1984) for the formation of the corona. Fig. 3 shows that the step-function ordering by FIP is more clearly defined in the new data, including the elements P, Cl, K, Ti, and Mn. However, Fig. 3 also discloses statistically significant enhancements and depletions of several elements such as Na, Fe and Ni, which are discussed by Breneman and Stone (1985) in the context of an acceleration/propagation fractionation of SEPs based on the ionic charge-to-mass ratio of the species making up the SEPs.

In Fig. 4, the SEP abundances are compared to galactic cosmic ray source (GCRS) abundances (Lund 1984). The absence of a FIP-dependence in the SEP/GCRS ratio indicates that the GCRS may have a FIP-dependent step-function fractionation like that of the SEPs (Cook et al. 1979, Meyer 1981, Lund 1984). Both may exhibit a depletion of elements with FIP greater than ~10 eV because of the smaller flux of ionizing photons with energies greater than that of Ly-α (10.2 eV). Both C and N appear to be distinctly different in SEPs and the GCRS.

Table I. SEP average elemental abundances (Si = 1000).

Z	abundance	Z	abundance	Z	abundance	Z	abundance
3	< 1.36	10	$887._{-83}^{+91}$	17	$2.01_{-0.82}^{+0.83}$	24	$14.3_{-2.4}^{+2.9}$
4	< 0.17	11	$73.3_{-6.6}^{+7.2}$	18	$20.7_{-3.0}^{+3.5}$	25	$5.0_{-1.9}^{+2.7}$
5	< 0.34	12	$1206._{-61}^{+64}$	19	$2.95_{-0.93}^{+1.01}$	26	$959._{-94}^{+105}$
6	$2710._{-240}^{+270}$	13	$87.4_{-4.1}^{+4.3}$	20	$68._{-10}^{+12}$	27	< 13.5
7	$775._{-51}^{+54}$	14	1000.	21	$(0.22_{-0.22}^{+0.38})$*	28	$33.6_{-5.3}^{+6.0}$
8	$6230._{-540}^{+360}$	15	$4.78_{-0.70}^{+0.84}$	22	$3.5_{-1.1}^{+1.4}$	29	$(0.40_{-0.40}^{+0.64})$*
9	$(0.29_{-0.29}^{+0.29})$*	16	$222._{-7}^{+8}$	23	$(0.34_{-0.34}^{+0.48})$*	30	$1.09_{-0.89}^{+0.92}$

* Abundances for these elements are based on fewer than 5 particles and are highly uncertain.

3

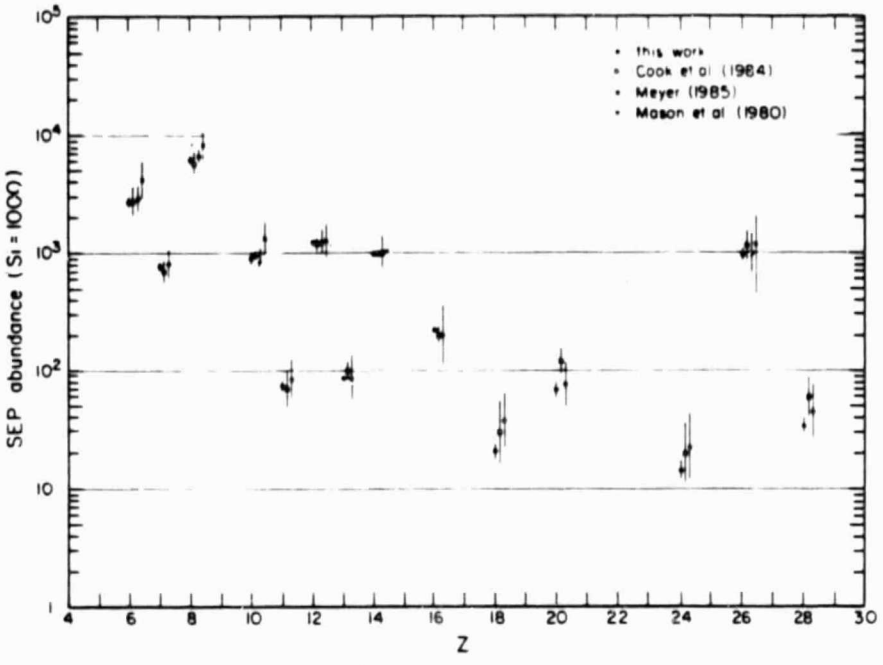

Fig. 2. Comparison of the new SEP abundances with other recent SEP abundance measurements.

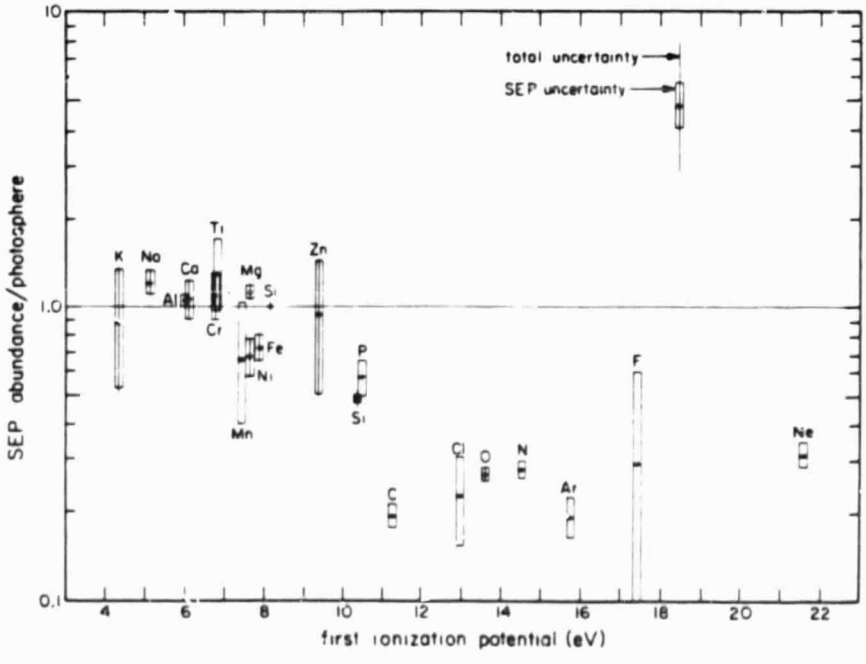

Fig. 3. SEP abundances (Si = 1) relative to spectroscopic photospheric abundances (Grevesse 1984), plotted vs. FIP.

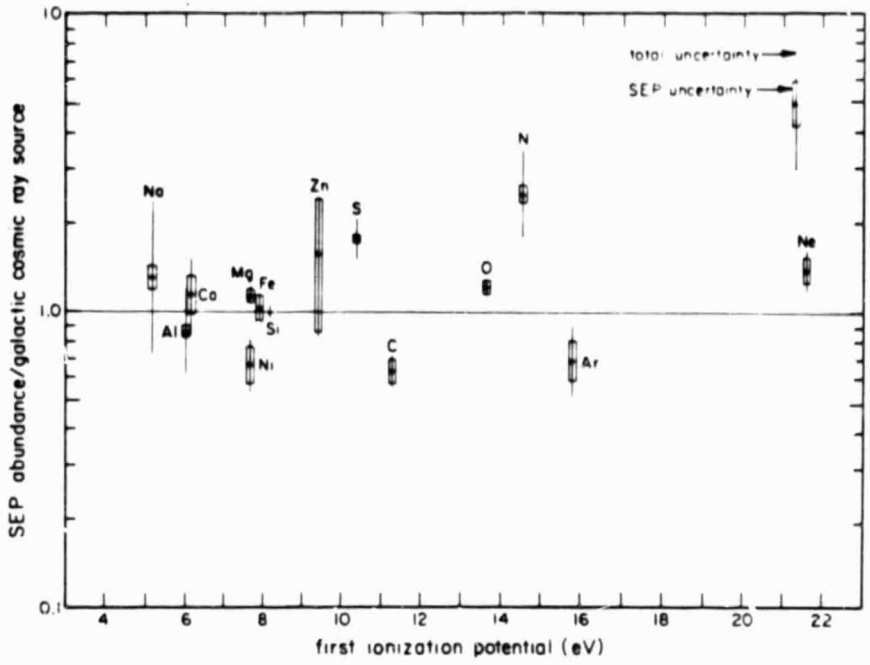

Fig. 4. SEP abundances (Si = 1) relative to galactic cosmic ray source abundances (Lund 1984), plotted vs. FIP.

5. Acknowledgements

This work has been supported in part by the National Aeronautics and Space Administration under contract NAS7-918 and grant NGR 05-002-160.

References

Breneman, H., and Stone, E. C. 1985, *Proc. 19th Int. Cosmic Ray Conf.* (La Jolla), paper SH 2.1-5.

Cook, W. R., Stone, E. C., Vogt, R. E., Trainor, J. H., and Webber, W. R. 1979, *Proc. 16th Int. Cosmic Ray Conf.* (Kyoto), **12**, 265.

Cook, W. R., Stone, E. C., and Vogt, R. E. 1984, *Ap. J.* **279**, 827.

Geiss, J., and Bochsler, P. 1984, International Conference on Isotopic Ratios in the Solar System, Paris.

Grevesse, N. 1984, *Physica Scripta* **T8**, 49.

Hovestadt, D. 1974, in *Solar Wind III*, ed. by C. T. Russell, University of California, Los Angeles.

Lund, N. 1984, Invited Lecture at the Symposium on Nucleosynthesis and Acceleration of Cosmic Rays, XXV COSPAR Plenary Meeting, Graz, Austria.

Mason, G. M., Fisk, L. A., Hovestadt, D., and Gloeckler, G. 1980, *Ap. J.* **239**, 1070.

McGuire, R. E., von Rosenvinge, T. T., and McDonald, F. B. 1979, *Proc. 16th Int. Cosmic Ray Conf.* (Kyoto), **5**, 61.

Meyer, J.-P. 1981, *Proc. 17th Int. Cosmic Ray Conf.* (Paris), **3**, 145.

Meyer, J.-P. 1985, *Ap. J. Suppl.* **57**, 151.

Stone, E. C., Vogt, R. E., McDonald, F. B., Teegarden, B. J., Trainor, J. H., Jokipii, J. R., and Webber, W. R. 1977, *Sp. Sci. Rev.* **21**, 355.

Webber, W. R. 1975, *Proc. 14th Int. Cosmic Ray Conf.* (Munich), **5**, 1597.

Solar Coronal and Photospheric Abundances from Solar Energetic Particle Measurements

H. Breneman and E. C. Stone

California Institute of Technology
Pasadena, California 91125 USA

1. Introduction

Solar energetic particle (SEP) elemental abundance data from the Cosmic Ray Subsystem (CRS) aboard the Voyager 1 and 2 spacecraft (Breneman and Stone 1985) are used to derive unfractionated coronal and photospheric abundances for elements with $3 \leq Z \leq 30$. We find that the ionic charge-to-mass ratio (Q/M) is the principal organizing parameter for the fractionation of SEPs by acceleration and propagation processes and for flare-to-flare variability, making possible a single-parameter Q/M-dependent correction to the average SEP abundances to obtain unfractionated coronal abundances. A further correction based on first ionization potential allows the determination of unfractionated photospheric abundances.

2. Results

The composition of individual flares relative to the average SEP composition can be described by a function that is roughly monotonic in Z but variable in magnitude from flare to flare (Cook et al. 1979, 1984; McGuire et al. 1979; Meyer 1981,

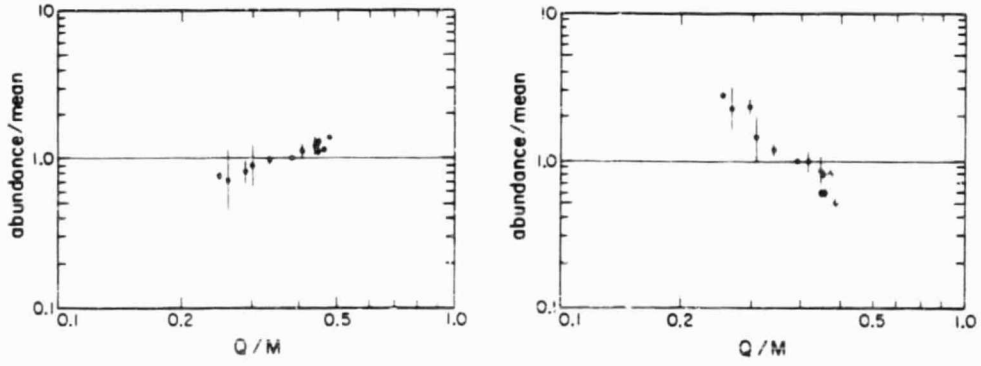

Fig. 1. Abundances relative to the mean SEP abundance for two typical flares, plotted vs. Q/M.

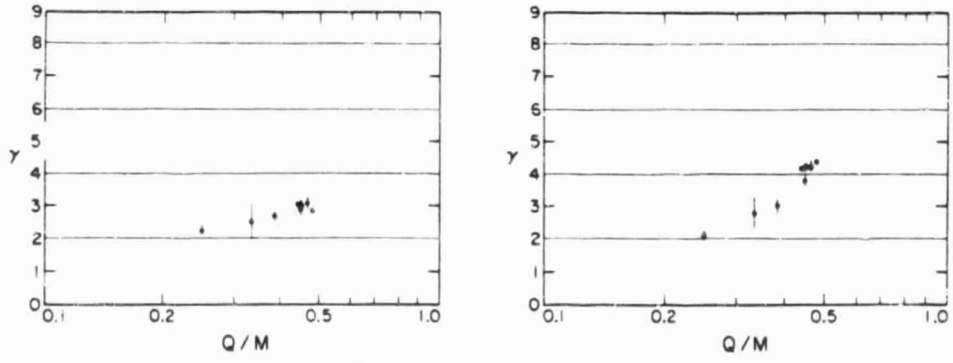

Fig. 2. Spectral index γ vs. Q/M for two typical flares.

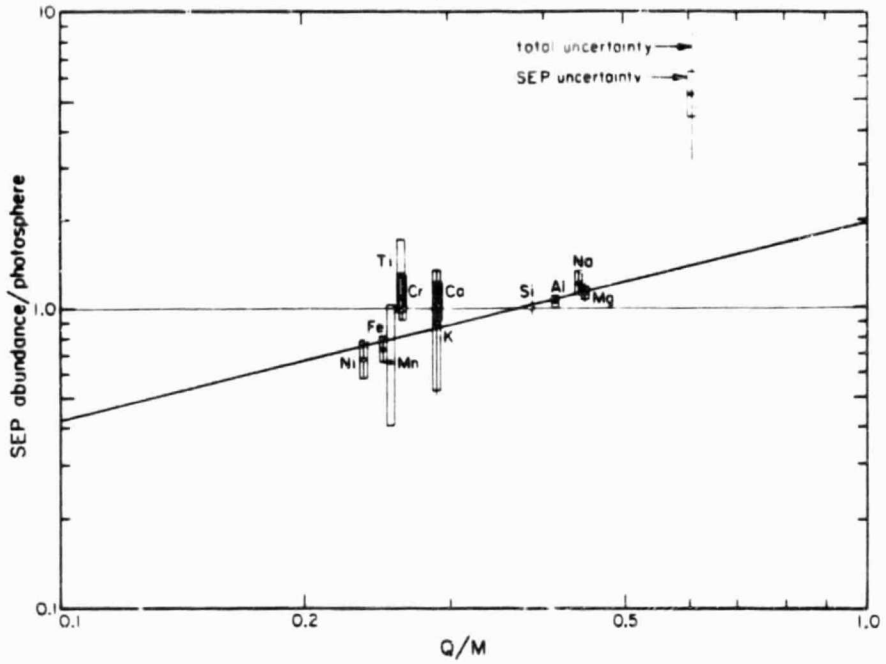

Fig. 3. Mean SEP abundance relative to the photosphere (Grevesse 1984) for the low-FIP elements, plotted vs. Q/M. The best-fit power-law has a reduced χ^2 of 1.0.

1985). Using the recently reported SEP ionic charge states (Luhn et al. 1984), we find that this compositional variability exhibits a monotonic dependence on the ionic charge-to-mass ratio Q/M of the particles, as illustrated in Fig. 1. Such a dependence is not unexpected for acceleration and propagation effects. The spectral indices of the elemental differential energy spectra for a given flare also tend to be ordered by Q/M (Fig. 2). Thus we derive an unfractionated coronal composition by applying a Q/M-dependent correction to the average SEP abundances.

3. Discussion

The correction factor has been determined by comparing the SEP abundances of elements with low first ionization potential (FIP), which display no FIP-dependent fractionation (Breneman and Stone 1985), to the photospheric spectroscopic abundances (Grevesse 1984) (see Fig. 3). The derived correction function, which is a power-law in Q/M with a slope of 0.66 ± 0.17, may be applied to the SEP abundances for *all* elements, resulting in SEP-derived coronal abundances (see Table I). As Fig. 4 shows, they agree well with coronal abundances obtained by XUV/X-ray spectroscopy, but have much higher precision and are available for many more elements.

The derived coronal abundances can also be corrected for the FIP-dependent fractionation suggested by the dynamical ionization model of Geiss and Bochsler (1984). In this model, the high-FIP elements such as N, O, F, Ne, Cl and Ar are depleted because their ionization times are longer than the time individual atoms spend in a rising spicule. Thus, their abundances are corrected by the depletion factor of oxygen in SEPs relative to the photosphere (4.03 ± 0.26); P and S are corrected by the depletion factor of sulfur (1.89 ± 0.17); C is corrected by the mean of the oxygen and sulfur depletion factors, since its proper depletion factor is uncertain; and the low-FIP elements, which are quickly ionized, are left

Table I. SEP-derived coronal and photospheric abundances relative to silicon

Z	SEP-derived corona	SEP-derived photosphere	Z	SEP-derived corona	SEP-derived photosphere
6	$2350._{-230.}^{+260.}$	$6490._{-270.}^{+280.}$	19	$3.9_{-1.6}^{+2.1}$	$3.9_{-1.6}^{+2.1}$
7	$700._{-40.}^{+52.}$	$2775._{-60.}^{+63.}$	20	$82._{-12.}^{+14.}$	$82._{-12.}^{+14.}$
8	$5680._{-340.}^{+360.}$	22900.	21	$(0.31_{-0.31}^{+0.55})$*	$(0.31_{-0.31}^{+0.55})$*
9	$(0.28_{-0.28}^{+0.29})$*	$(1.1_{-1.1}^{+1.2})$*	22	$4.9_{-1.3}^{+1.6}$	$4.9_{-1.3}^{+1.6}$
10	$783._{-77.}^{+84.}$	$3140._{-195.}^{+205.}$	23	$(0.48_{-0.48}^{+0.69})$*	$(0.48_{-0.48}^{+0.69})$*
11	$67.0_{-6.2}^{+6.8}$	$67.0_{-6.2}^{+6.8}$	24	$18.3_{-3.3}^{+3.9}$	$18.3_{-3.3}^{+3.9}$
12	$1089._{-82.}^{+84.}$	$1089._{-82.}^{+84.}$	25	$6.8_{-2.7}^{+3.9}$	$6.8_{-2.7}^{+3.9}$
13	$83.7_{-4.0}^{+4.2}$	$83.7_{-4.0}^{+4.2}$	26	$1270._{-150.}^{+170.}$	$1270._{-150.}^{+170.}$
14	1000.	1000.	27	< 18.1	< 18.1
15	$4.89_{-0.72}^{+0.86}$	$9.24_{-1.54}^{+1.46}$	28	$46.5_{-7.4}^{+8.1}$	$46.5_{-7.4}^{+8.1}$
16	$242._{-9.}^{+10.}$	$460._{-39.}^{+42.}$	29	$(0.57_{-0.57}^{+0.87})$*	$(0.57_{-0.57}^{+0.87})$*
17	$2.38_{-0.80}^{+0.84}$	$9.6_{-3.5}^{+3.5}$	30	$1.61_{-0.76}^{+0.87}$	$1.61_{-0.76}^{+0.87}$
18	$24.1_{-3.6}^{+4.2}$	$102._{-17.}^{+20.}$			

* Based on fewer than 5 particles and highly uncertain.

unchanged. The resulting SEP-derived photospheric abundances (Table I) involve fewer modeling parameters than spectroscopic determinations and are available for some elements (e.g., C, N, Ne, Ar) that cannot be observed spectroscopically. The main differences (Fig. 5) are a significantly higher abundance of Cr (and possi-

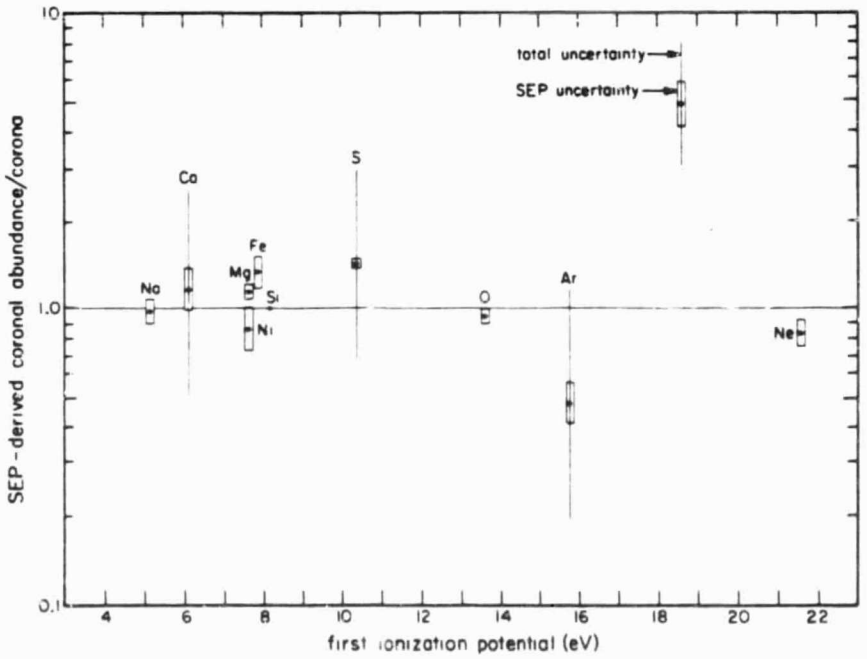

Fig. 4. SEP-derived coronal abundances relative to spectroscopically-derived coronal abundance (Veck and Parkinson 1981), plotted vs. FIP.

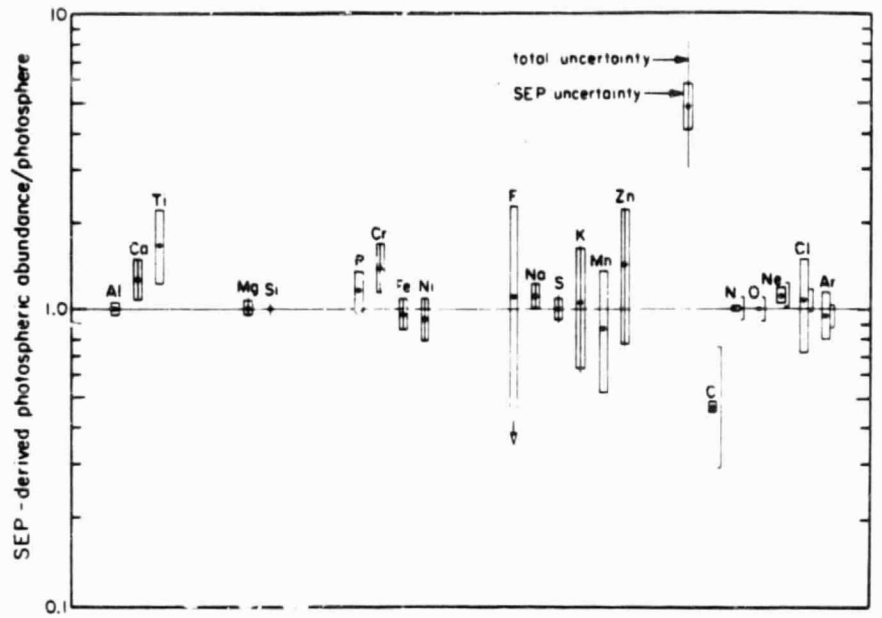

Fig. 5. SEP-derived photospheric abundances relative to spectroscopically-derived photospheric abundances (Grevesse 1984). The estimated uncertainty in the FIP fractionation correction is indicated by the vertical brackets.

bly Ca and Ti) and a C abundance that is about half of the commonly assumed solar abundance. The SEP-derived Fe/Si ratio is in agreement with the recent photospheric value (Grevesse 1984), which is 50% larger than the meteoritic value.

4. Acknowledgements

This work has been supported in part by the National Aeronautics and Space Administration under contract NAS7-918 and grant NGR 05-002-160.

References

Breneman, H., and Stone, E. C. 1985, *Proc. 19th Int. Cosmic Ray Conf.* (La Jolla), paper SH 2.1-4.

Cook, W. R., Stone, E. C., Vogt, R. E., Trainor, J. H., and Webber, W. R. 1979, *Proc. 16th Int. Cosmic Ray Conf.* (Kyoto), **12**, 265.

Cook, W. R., Stone, E. C., and Vogt, R. E. 1984, *Ap. J.* **279**, 827.

Geiss, J., and Bochsler, P. 1984, International Conference on Isotopic Ratios in the Solar System, Paris.

Grevesse, N. 1984, *Physica Scripta* **T8**, 49.

Luhn, A., Klecker, B., Hovestadt, D., Gloeckler, G., Ipavich, F. M., Scholer, M., Fan, C. Y., and Fisk, L. A. 1984, *Adv. Space Res.* **4**, No. 2-3, 161.

McGuire, R. E., von Rosenvinge, T. T., and McDonald, F. B. 1979, *Proc. 16th Int. Cosmic Ray Conf.* (Kyoto), **5**, 61.

Meyer, J.-P. 1981, *Proc. 17th Int. Cosmic Ray Conf.* (Paris), **3**, 145.

Meyer, J.-P. 1985, *Ap. J. Suppl.* **57**, 151.

D10

SH 4.1-13

ABST. ONLY

N85-33054

LATITUDE VARIATION OF RECURRENT FLUXES IN THE OUTER SOLAR SYSTEM

S. P. Christon and E. C. Stone
California Institute of Technology, USA

(Confirming Abstract)

Recurrent low-energy ($\gtrsim$ 0.5 MeV) proton flux enhancements, reliable indicators of corotating plasma interaction regions, were observed on the Voyager 1 and 2 and Pioneer 11 spacecraft in the heliographic latitude range 2°S to 23°N and the heliocentric radial range 11 to 20 AU [Christon and Stone, 1985]. After a period of rather high correlation between fluxes at different latitudes in early 1983, distinct differences developed in the fluxes during an overall flux decrease. The flux intensities returned to higher levels in early 1984 and differences in both the recurrence frequency and flux intensity persisted into 1985, as Voyager 1 traveled to 23 AU and 25°N latitude. Intercomparison of data from the three spacecraft indicates that the flux differences are most likely due to latitudinal, rather than radial or temporal, variations.

References.

Christon, S.P. and E.C. Stone [1985], *Geophys. Res. Lett.*, *12*, 109.

D11 SH 4.2-9
N85-33055

DIFFERENTIAL MEASUREMENT OF COSMIC-RAY GRADIENT WITH RESPECT TO INTERPLANETARY CURRENT SHEET

S. P. Christon, A. C. Cummings, and E. C. Stone
California Institute of Technology

K. W. Behannon, and L. F. Burlaga
Goddard Space Flight Center

ABSTRACT

Simultaneous magnetic field and charged particle measurements from the Voyager spacecraft at heliographic latitude separations from 10° to 21° are used to determine the latitude gradient of the galactic cosmic ray flux with respect to the interplanetary current sheet. By comparing the ratio of cosmic ray flux at Voyager 1 to that at Voyager 2 during periods when both spacecraft are first north and then south of the interplanetary current sheet, we find an estimate of the latitudinal gradient with respect to the current sheet of approximately -0.15 ± 0.05 %/deg under restricted interplanetary conditions.

1. **Introduction.** Organization of cosmic ray flux about the heliographic equator should result from symmetries in the interplanetary magnetic field produced by the sun's rotation. However, if particle drifts are important in cosmic ray transport, the cosmic ray flux should be organized with respect to the interplanetary current sheet. This symmetrizing property of the current sheet has been demonstrated in a three-dimensional model of cosmic ray transport including particle drifts [Kota and Jokipii, 1983]. At 1 AU, gradients with respect to the current sheet G_ϕ of up to ~ -0.33 %/deg have been identified for cosmic ray protons with energies >100 MeV in various integral energy ranges [Newkirk et al., 1984; Newkirk and Fisk, 1985].

The interplanetary current sheet is a surface separating regions of magnetic field pointing generally toward or away from the sun. In its least complicated configuration, the near-sun current sheet is essentially a circle tilted with respect to the heliographic equator. As the rotating sun's magnetic field is drawn out by the solar wind, warping of the current sheet ensues, thus allowing two spacecraft separated in latitude to sample fluxes on either side of it (Figure 1). The near-sun current sheet extends up to ~60° north N and south S of the equator and produces an interplanetary sector pattern that varies between two and four sectors during the period of this study [Hoeksema, 1984].

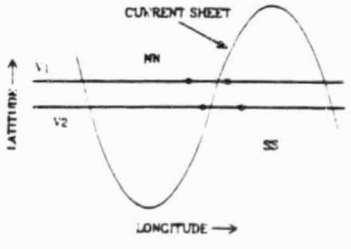

Fig. 1. Schematic representation of NN and SS configuration.

We determine G_ϕ using spacecraft trajectory information, the ratio of cosmic ray flux, and observations of the current sheet (magnetic field sector boundaries) at Voyager 1 (V1) and Voyager 2 (V2), separated in latitude by 10° to 21°. Such a differential measurement has significantly smaller non-latitudinal intensity variations than a single-point measurement such as the type employed by Newkirk et al. and Newkirk and Fisk. The cosmic ray flux at an observation point in the heliosphere is $j = j_b \exp(G_r(r-R_b))\exp(G_\theta(\Theta-\Theta_{cs}))$, where G_r is the radial gradient, G_θ is the colatitude gradient with respect to the current sheet, R_b is the radius of the boundary of the heliosphere, j_b is the cosmic ray flux at R_b, assumed constant, Θ_{cs} is the colatitude of the current sheet, and r and Θ are the radius and colatitude of the observation point. Heliographic colatitudes Θ from 0° to 180° correspond to

heliographic latitudes from 90°N to 90°S. Time series of simultaneous observations at two points in interplanetary space well separated in latitude allow estimates of G_θ to be obtained for each interval in the series. These individual estimates of $G_\theta = (\ln\Gamma - G_r\,(r_1 - r_2))/(\theta_1 - \theta_2)$, where the subscripts 1 and 2 refer to V1 and V2, respectively, and Γ is the ratio of the flux at V1 to that at V2, are independent of variations in the separation of the observation points. Statistically weighted averages of $\langle G_\theta \rangle_{NN(SS)} = \sum_{i(j)} w_{\theta i(j)} G_{\theta i(j)} / \sum_{i(j)} w_{\theta i(j)}$ and $\langle G_\theta \rangle = \left[\sum_i w_{\theta i} G_{\theta i} - \sum_j w_{cj} G_{\theta j}\right] / \left(\sum_i w_{\theta i} + \sum_j w_{\theta j}\right)$, where i(j) runs from 1 to $n_{NN}(n_{SS})$, the number of observations when both spacecraft are north (NN) or both south (SS) of the current shee' The first character of the two character identifier represents the magnetic field region for V1, the second for V2. Data for NS and SN configurations are also collected and are used independently, and in combination with the NN and SS data, to estimate G_r.

2. Data Selection.

This study covers the period from day 240, 1981 until day 190, 1983. while the V1-V2 separation increased from 1.9 to 4.7 AU in radial distance from the sun and from 10° to 21° in latitude. V1 traveled from 11 to 17 AU and from 6°N to 20°N. V1-V2 longitude separation was ≤16°. Daily samples of counting rates of protons with energies >75 MeV and a median energy ~1.1 GeV measured by the nearly identical High Energy Telescopes of the Voyager Cosmic Ray Subsystem [Stone et al., 1977], and Γ the ratio of V1 to V2 counting rate samples are plotted in Figure 2. Calendar days for the NN and SS data sets are highlighted in the upper panel by underscoring. We have compared measurements taken at both spacecraft on the same day under the assumptions that convective effects are unimportant on the average, consistent with long-interval average observations [Venkatesan et al, 1983], and that local variations in the cosmic ray intensity, after eliminating solar flare transient effects, are due to variations in the distance to the current sheet [Newkirk and Fisk, 1985].

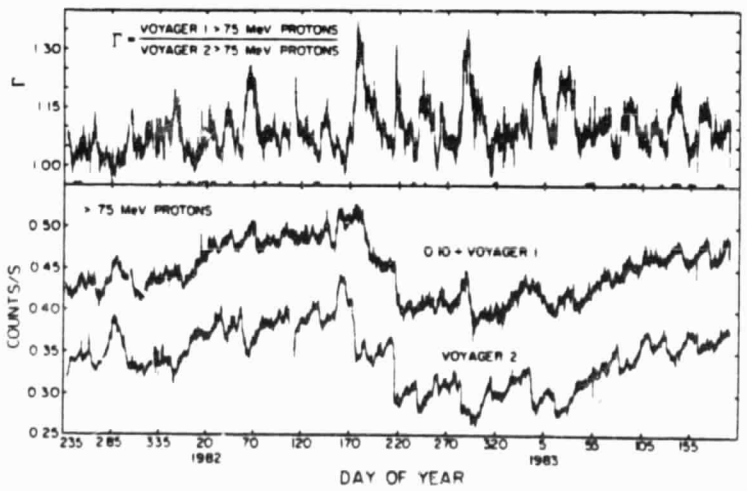

Fig. 2. Daily samples of the counting rates of >75 MeV protons from V1 and V2 (V1 is offset for clarity) and Γ the ratio of V1 to V2 counting rate samples. Uncertainties are due to counting statistics.

The counting rates of >75 MeV and ~1 MeV protons were used to eliminate periods possibly contaminated by solar flare particles and Forbush decreases. Proton energy spectra and elemental abundance measurements at lower energies were also used for this purpose. Hourly averages of the interplanetary magnetic field azimuth and elevation angles (Figure 3) measured by the Voyager Magnetic Field Experiment were used to determine the less active magnetic field periods, sector

polarities, and transition regions between sectors. Time blocks of data were identified when V1 and V2 were in regions of magnetic field pointing generally toward or away from the sun along the expected field direction, which is generally perpendicular to the radial direction in the outer solar system and parallel to the equatorial plane near the equator. The minimum sector length used herein is 4.5 days, so that V1 and V2 were most likely in field regions associated with plasma flows from the sun's polar coronal holes. This produced Data Set (DS) I. Then days with a poorly defined transition region at either end of the magnetic sector and days with azimuthal turbulence were eliminated in order to produce DS II. Finally, days with elevation angles pointing away from the equatorial region and days with elevation angle turbulence were collected into subset DS IIb. When the elevation angle changes by a large amount in less than a day or two as in DS IIb, it is likely to represent a dynamical effect such as the passage of transient material or perhaps reconnection at a sector boundary, either of which could alter the cosmic ray gradient. Those quietest days remaining are subset DS IIa.

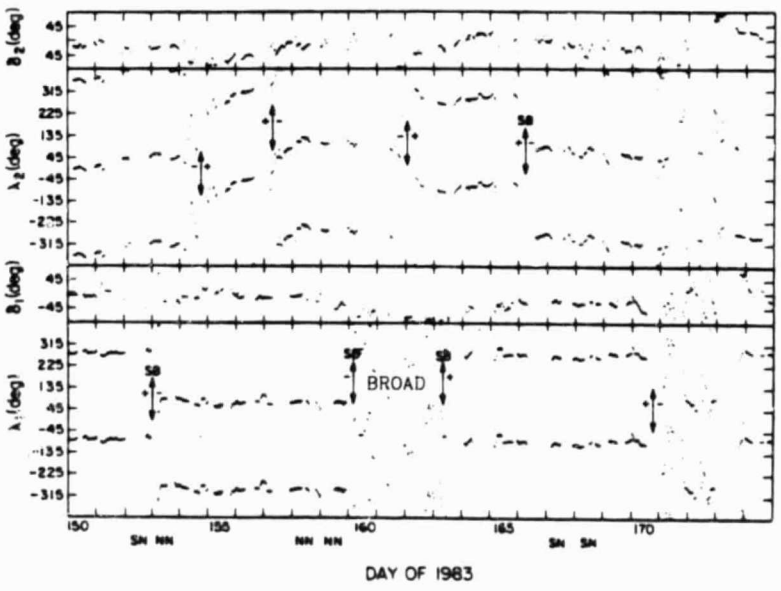

Fig. 3. Magnetic field azimuth and elevation angles from V1 and V2. The azimuth, λ, is 0° when the field is directed away from the sun and the elevation, δ, is 0° when the field is along the spacecraft-sun line. Two cycles of λ are plotted. Arrows highlight transition regions interpreted as current sheet crossings. Those labeled "SB" are similar to sector boundaries at 1 AU.

3. Observations and Discussion. Determination of $\langle G_\phi \rangle$ requires knowledge of the value of G_r, which can be estimated from NS and SN data sets, since the latitude gradients, which have opposite signs in the two hemispheres should average to zero. Averaged over NS and SN, $\langle G_r \rangle_{NSSN} = 2.21 \pm 0.11$ %/AU, consistent with radial gradients reported by [Venkatesan et al., 1983]. G_r can also be determined by averaging the NN and SS data sets, assuming that G_θ is negligible. This results in $\langle G_r \rangle_{NNSS} = 2.29 \pm 0.13$ %/AU, consistent with $\langle G_r \rangle_{NS,SN}$, and suggesting that the best estimate is the average over all 152 days of data which yields $\langle G_r \rangle = 2.25 \pm 0.08$ %/AU. Note that an uncertainty of 0.1 %/AU in the assumed G_r introduces an error of only 0.01 %/deg in the derived $\langle G_\phi \rangle$.

$\langle G_\theta \rangle$ and $\langle G_\phi \rangle$ have been calculated both without restrictions on spacecraft position (unrestricted average), and with restrictions on spacecraft position with respect to the current sheet based upon time to or from the closest sector boundary crossing (restricted average). Requiring V2 to be closer to the current sheet than V1 for NN data and V1 closer than V2 for SS data (see e.g., Figure 1), should enhance the measured $\langle G_\phi \rangle$.

4

Table 1 $\langle G_\theta \rangle$ and $\langle G_\phi \rangle$ (# days of observation)

unrestricted average

DS	$\langle G_\theta \rangle_{NN}$ (%/deg)	$\langle G_\theta \rangle_{SS}$ (%/deg)	$\langle G_\phi \rangle$ (%/deg)
I	0.02 ± 0.03 (52)	-0.02 ± 0.04 (22)	0.02 ± 0.03 (74)
II	0.03 ± 0.04 (29)	-0.01 ± 0.04 (19)	0.02 ± 0.03 (48)
IIa	-0.02 ± 0.05 (21)	-0.06 ± 0.03 (6)	-0.01 ± 0.04 (27)
IIb	0.14 ± 0.09 (8)	0.01 ± 0.05 (13)	0.06 ± 0.05 (21)

restricted average

DS	$\langle G_\theta \rangle_{Nn}$ (%/deg)	$\langle G_\theta \rangle_{sS}$ (%/deg)	$\langle G_\phi \rangle$ (%/deg)
I	-0.12 ± 0.04 (21)	0.09 ± 0.07 (7)	-0.11 ± 0.03 (28)
II	-0.18 ± 0.05 (10)	0.12 ± 0.09 (5)	-0.16 ± 0.04 (15)
IIa	-0.18 ± 0.05 (10)	-0.06 ± 0.08 (1)	-0.15 ± 0.05 (11)
IIb	---------- (0)	0.20 ± 0.09 (4)	-0.20 ± 0.09 (4)

Table 1 lists values of $\langle G_\theta \rangle$ and $\langle G_\phi \rangle$ for both positional criteria (the lower case subscript is for the spacecraft closer to the current sheet) using G_r = 2.25 %/AU for the radial gradient correction. Note that the unrestricted $\langle G_\phi \rangle$ displays no observable gradient, while the restricted $\langle G_\phi \rangle$ is statistically significant and is approximately -0.15 ± 0.05 %/deg. Since differences between DS IIa and DS IIb are statistically insignificant, we have no evidence that field elevation turbulence affected our measurements. Figure 4 shows the separation of the Nn and sS subsets for DS II with the restricted average. Note that, even with such a small data set, a separation of means and modes of the Nn and sS distributions, attributable to a small, negative latitude gradient, is evident. Further studies are required to determine whether such gradients are typical of other time periods.

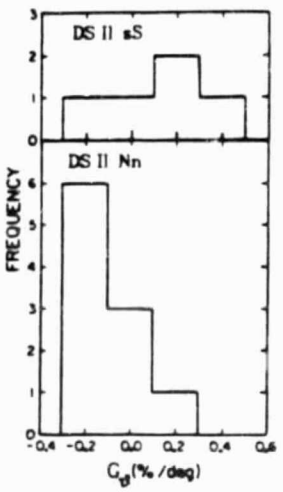

Fig. 4. $\langle G_\phi \rangle$ for DS II, restricted average.

4. Acknowledgements. We are grateful for the contributions of R.E. Vogt, other Voyager Cosmic Ray Subsystem team members, and N.F. Ness. Work at Caltech was supported in part by the National Aeronautics and Space Administration under contract JPL 49-556-63120-0-2600 and grant NGR 05-002-160.

References

Decker, R. B., S. M. Krimigis, and D. Venkatesan [1984], *Astrophys. J. Lett.*, *278*, L119.
Hoeksema, J. T. [1984], *Ph.D. Thesis*, Stanford University, Stanford CA.
Kota, J and J. R. Jokipii [1983], *Astrophys. J.*, *265*, 573.
Newkirk, G., J. Lockwood, M. Garcia-Munoz, and J. A. Simpson [1984], *EOS, Trans, Am. Geophys. U.*, *65*, 1034.
Newkirk, G. and L. A. Fisk [1985], *J. Geophys. Res.*, *90*, 3391.
Venkatesan, D., Decker, R. B., and S. M. Krimigis [1984], *J. Geophys. Res.*, *89*, 3735.

Changes in the Energy Spectrum of Anomalous Oxygen and Helium During 1977-1985

A. C. Cummings and E. C. Stone

California Institute of Technology, Pasadena, CA 91125 USA

W. R. Webber

University of New Hampshire, Durham, NH 03824 USA

We have used data from the cosmic-ray experiment on the Voyager spacecraft to measure the energy spectrum of anomalous O and He during the period 1977 to 1985. We find that these spectra change dramatically after the middle of 1980, with the peak or plateau region of the differential spectrum shifting to a higher energy. This change appears to be related to the reversal of the solar magnetic field and could imply that particle drifts are important to the acceleration or propagation of these particles.

1. Introduction. The study of the anomalous component of cosmic rays over the solar cycle may prove to be key to the understanding of the role of drifts in cosmic-ray modulation. *Pesses et al.* [1981] have suggested that the acceleration site of the anomalous component is most likely in the polar regions of the solar wind termination shock. In their model the particles drift latitudinally toward the neutral sheet from the polar regions during the last solar cycle, but drift radially inward along the neutral sheet during the current solar cycle. Consequently, they predict a strong dependence of the intensity of the anomalous component near the solar equator on solar magnetic field polarity. In this analysis we make use of measurements of the spectra of O and He from the Cosmic Ray Subsystem (CRS) [*Stone et al.*, 1977] on the Voyager 1 (V1) and 2 (V2) spacecraft to address whether or not these spectra exhibit changes associated with the polarity of the solar magnetic field.

2. Observations. The general features of the 11-year cosmic-ray modulation cycle are evident in the counting rate of the particles which penetrate the high energy telescope on V1, shown in Fig. 1 for 1977-1985. In order to minimize the contamination by solar and interplanetary energetic particles, quiet times were selected by setting limits to the maximum low-energy He flux, in a manner similar to that described in *Cummings et al.* [1984]. The six quiet-time periods that were selected for analysis for V1 are shown as horizontal bars in Fig. 1 and are labeled A through F. Also shown are the approximate times of the reversal of the solar polar magnetic fields [*Webb et al.*, 1984]. Note that the field reversal occurs approximately between periods C and D.

The anomalous O spectrum for the Voyager measurements is derived from the observed total O spectrum for a particular time interval by subtracting a low-energy solar or interplanetary component and the high-energy galactic cosmic-ray component. This subtraction procedure is illustrated in Fig. 2 for two extreme examples. The low-energy component is scaled and extrapolated from a power-law fit to the observed He spectrum in the energy range 3-6.1 MeV/nuc using a ratio He/O = 100 ± 50 (see *Gloeckler et al.* [1979]). The galactic cosmic-ray O component is estimated by normalizing the observed carbon spectrum to the O intensity in the 66-125 MeV/nuc energy interval.

Figure 3 shows the spectra of anomalous O for the six quiet-time intervals A through F derived from the V2 observations in the manner just described. The a and b panels show the spectra for the three intervals before and after the solar magnetic field reversal in 1980, respectively. The spectra for intervals A, B, and C are essentially monotonic with a tendency to flatten into a peak or plateau at less than ~6 MeV/nuc. It is clear from Fig. 3b that the energy dependence of the spectra for the intervals after the field reversal (D, E, and F) is significantly different, having a peak or plateau at ~10-20 MeV/nuc.

A similar change in the energy spectrum is also apparent in the V1 data. In Fig. 4a we show the V1 observed O spectra for intervals B and F. The galactic cosmic-ray intensity is dom-

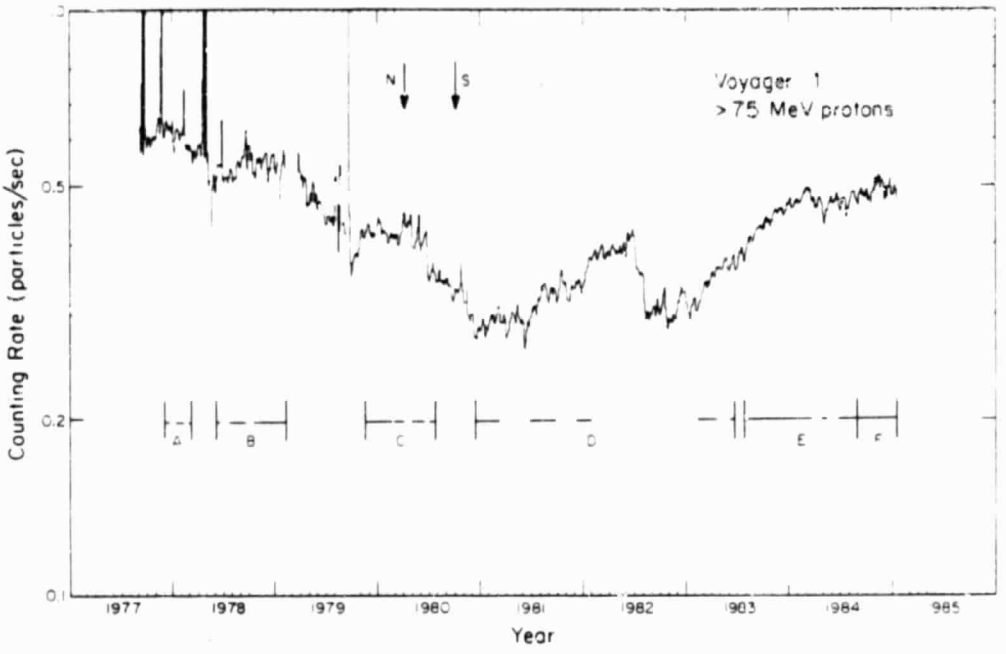

Fig. 1. Three-day average counting rate of penetrating particles in the HET 1 (High-Energy Telescope number 1) of the V1 CRS instrument from 1977 to 1986. The rate is dominated by protons with energy > 75 MeV. The bars and arrows are described in the text.

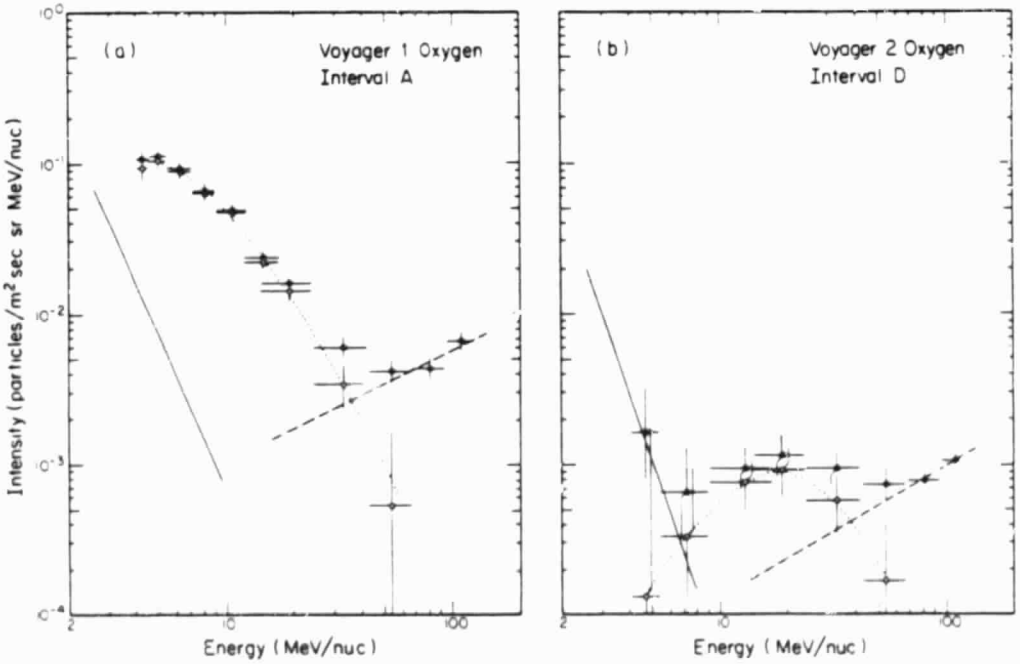

Fig. 2. Quiet-time energy spectra of O from Voyager data for two sample time intervals. The observed spectra are shown as the solid circles. Estimated spectra of interplanetary and galactic components are shown as solid and dashed lines, respectively. The spectra of anomalous O are indicated by the open squares which are joined by the dotted lines.

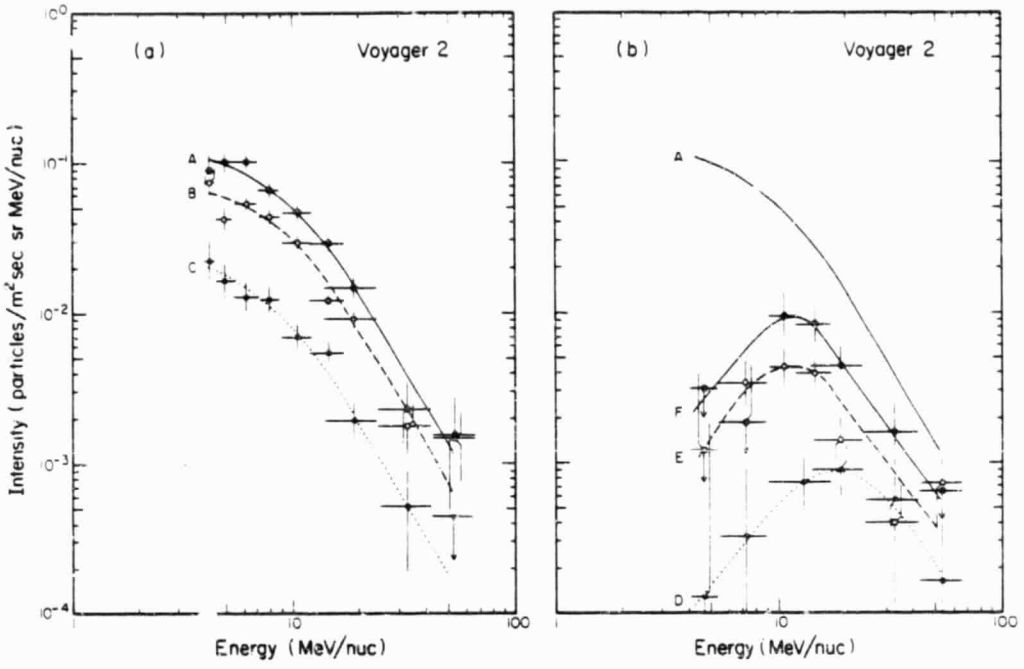

Fig. 3. Spectra of anomalous O from V2 for the six quiet-time intervals. Panels a and b show the spectra for periods before and after the solar magnetic field reversal, respectively. The smooth curves are drawn to aide the eye and are not functional fits to the data. The dashed line labeled "A" in panel b is copied from panel a to facilitate comparison. Note the higher energy of the peak (or plateau) intensity of the spectra in panel b when compared to those of panel a.

inant in the 50-125 MeV/nuc energy range for both time intervals. The intensity in this energy range is only ~20% higher for interval B than for interval F, indicating that a similar level of modulation has been reached. Similarly, the anomalous O intensity in the 10-30 MeV/nuc energy range is approximately the same for the two time intervals. However, below 10 MeV/nuc there is a factor of 10 difference in intensity producing a striking difference in the spectrum.

This change in the energy spectrum is also evident in the He data. We show in Fig. 4b the observed He spectrum for the same two intervals as for Fig. 4a. Below ~8 MeV/nuc a low-energy solar or interplanetary component is dominant and causes a sharp upturn in the spectrum. For interval B the flat region of the spectrum from ~8 to 50 MeV/nuc indicates that anomalous He is the primary component, dominating the flux of solar and galactic cosmic rays. The period F spectrum has a much lower intensity than the period B spectrum below ~30 MeV/nuc suggesting that the anomalous He spectrum has shifted to higher energies. If the particles are singly ionized, the energy dependence of the He spectrum is expected to be obtained by shifting the anomalous O spectrum by a factor of ~4 in energy [*Cummings et al.*, 1984], so that the absence of anomalous He below 30 MeV/nuc is consistent with the reduced intensity of anomalous O below 8 MeV/nuc.

3. **Discussion.** If the changes in the energy spectra of the anomalous component are to be explained by "conventional" modulation theory, in which the effects of diffusion, convection, and adiabatic deceleration are considered, and the effects of drifts ignored (see *Fisk* [1980], for a review of solar modulation theory), then it would require either a very prolonged "hysteresis" effect or a significant change in the rigidity dependence of the diffusion coefficient between halves of the solar cycle. A hysteresis effect (phase-lag between intensity variations of low-rigidity and high-rigidity particles) has been reported for the anomalous O component by *Klecker et. al* [1980] for the 1974-1975 period. They found a phase lag of 72 days between the intensity of

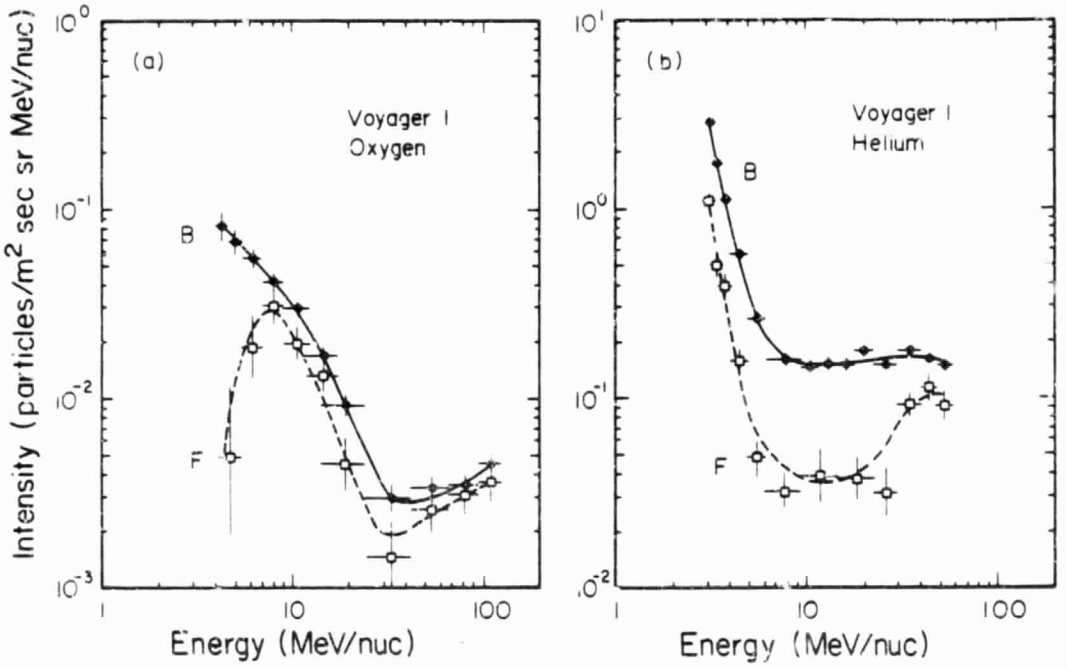

Fig. 4. Spectra of observed O (a) and He (b) for time intervals B and F from V1.

anomalous O with 7.6-24 MeV/nuc and the intensity of galactic cosmic rays with energy > 10GeV. If the energy spectrum changes in our study are to be ascribed to hysteresis, then a phase lag of ~4 years would be required between particles with only modestly different rigidities and velocities. If changes in the diffusion coefficient between halves of the solar cycle are to account for our observations then the spectra of other cosmic-ray species would show pronounced effects at the corresponding rigidities.

It appears more likely, therefore, that the observed time variation of the energy spectra of anomalous O and He may be related to changes in the acceleration of particles at the termination shock due to the change in the polarity of the solar magnetic field. Recently, *Jokipii* [1985] has used a model of the anomalous component which includes acceleration at the termination shock and particle drifts and has calculated spectra of anomalous O and He in the two halves of the solar cycle with different field polarity that resemble the observations reported here.

4. Acknowledgments. We are grateful to R. E. Vogt and other CRS team members at the California Institute of Technology, the Goddard Space Flight Center, the University of Arizona, and the University of New Hampshire. This work was supported in part by NASA under contract NAS 7-918 and grant NGR 05-002-160.

5. References.

Cummings, A. C., E. C. Stone, and W. R. Webber, *Ap. J. (Letters), 287*, L99, 1984.

Fisk, L. A., *Proc. Conf. Ancient Sun*, edited by R. O. Pepin, J. A. Eddy, and R. B. Merrill, (Pergamon Press : New York), 103, 1980.

Gloeckler, G., D. Hovestadt, and L. A. Fisk, *Ap. J. (Letters), 230*, L191, 1979.

Jokipii, J. R., submitted to *J. Geophys. Res.*, 1985.

Klecker, B., D. Hovestadt, G. Gloeckler, and C. Y. Fan, *Geophys. Res. Letters, 7*, 1033, 1980.

Pesses, M. E., J. R. Jokipii, and D. Eichler, *Ap. J. (Letters), 246*, L85, 1981.

Stone, E. C., R. E. Vogt, F. B. McDonald, B. J. Teegarden, J. H. Trainor, J. R. Jokipii, and W. R. Webber, *Space Sci. Rev., 21*, 355, 1977.

Webb, D. F., J. M. Davis, and P. S. McIntosh, *Solar Phys., 92*, 109, 1984.

SOLAR CYCLE VARIATIONS OF THE ANOMALOUS COSMIC RAY COMPONENT

R. A. Mewaldt and E. C. Stone

California Institute of Technology
Pasadena, California 91125 USA

The intensity of the "anomalous" cosmic ray component, consisting of He, N, O, and Ne, has long been known to be especially sensitive to the effects of solar modulation. Following its discovery in 1972, this component dominated the quiet-time flux of cosmic ray nuclei below ~30 MeV/nucleon during the 1972-1978 solar minimum, but then became essentially unobservable at 1 AU with the approach of solar maximum conditions. One recent theoretical model predicts substantial differences in the intensity of the anomalous fluxes from one solar minimum period to the next because of the reversal of the solar magnetic field. Using data from the Caltech experiments on IMP-8 and ICE (ISEE-3), we report on the intensity of anomalous O and He at 1 AU during the years 1972 to 1985. In particular, we hope to determine whether the anomalous fluxes will return to their 1972-1978 levels, as predicted by spherically symmetric modulation models, or whether they will fail to return to 1 AU, as suggested by modulation models in which gradient and curvature drifts dominate.

Our preliminary analysis of data from 1984 shows that the intensity of 8 to 27 MeV/nucleon O is still more than an order of magnitude below its 1972 to 1978 levels, while the intensity of 25 to 43 MeV/nucleon He is a factor of ~8 below its maximum level in 1977. Data from 1985 is now being analyzed.

This work was supported in part by NASA under grant NGR 05-002-160 and contracts NAS5-28441 and NAS5-28449.

D-14

Radial and Latitudinal Gradients of Anomalous Oxygen During 1977-1985

W. R. Webber

University of New Hampshire, Durham, NH 03824 USA

A. C. Cummings and **E. C. Stone**

California Institute of Technology, Pasadena, CA 91125 USA

We find that the radial gradient of anomalous O remains constant during 1977-85 at -10-15%/AU although the intensity changes by more than a factor of 100. These results can be used to deduce that most of the modulation of the intensities of these particles is occurring beyond 27 AU. We also find evidence for a latitudinal gradient of $-+3$%/degree at low energies (7.1-10.6 MeV/nuc).

1. Introduction. In this analysis we make use of measurements of the spectrum of O nuclei from the Cosmic Ray Subsystem (CRS) on the Voyager 1 (V1) and 2 (V2) spacecraft [*Stone et al.*, 1977] and from the Goddard-University of New Hampshire experiment on Pioneer 10 [*McDonald et al.*, 1977] to study the radial and latitudinal gradients and temporal variations of anomalous O. Quiet-time data from 1977 to 1985 are utilized.

2. Observations. The general features of the 11-year cosmic-ray modulation cycle may be examined by using the counting rate of particles which penetrate the high-energy telescope on V1 as shown in Fig. 1 (curve "P", mainly protons > 75 MeV). A change in this rate by a factor ~ 2 is observed between 1977 and the minimum in 1981-82. This change is mainly due to solar modulation; however, some gradient effects are present in the data as well since V1 is moving outward from 1 to ~ 22 AU during this time period. Figure 1 also shows a similar plot for 40-106 MeV/nuc C+O nuclei for 24 quiet-time intervals between 1977-85 (curve "C+O"). Here the change in intensity between 1977 and the minimum in 1981 is a factor ~ 5. Finally, in Fig. 1 the temporal variations for 5.6-17.2 MeV/nuc anomalous O are shown for the same 24 quiet-time intervals (curve "O"). All three components show a similar pattern of variations but for the anomalous O the overall intensity variation is larger than the others, approaching a factor ~ 100.

In order to minimize contamination by solar and interplanetary particles and to help separate temporal and radial variations, six quiet-time intervals labeled A-F in Fig. 1 were selected by setting limits to the maximum low-energy helium flux, in a manner similar to that described in *Cummings et al.* [1984]. The anomalous O spectrum is derived from the observed total O spectrum for a particular time interval by subtracting both a low-energy solar or interplanetary component and the high-energy galactic cosmic-ray component [*Cummings et al.*, 1985].

In Fig. 2a, b, c we show the differential intensities of anomalous O nuclei in three separate energy intervals for each of the six quiet-time intervals at each of the spacecraft as they moved outward from the sun. The solid lines are least-squares fits to the data points, except for the lowest energy interval for periods E and F when V1 is at ~ 24 degrees north heliographic latitude. (V1 left the ecliptic plane after encounter with Saturn in 1980.) In these two cases the V1 points, connected by the dashed lines, are significantly above the straight lines (representing a constant radial gradient) connecting the V2 and P10 points. We attribute the deviation to a latitude gradient at low energies having a weighted average value of 3.0 ± 1.0%/degree for the combined two periods E and F.

In Fig. 3 we show the calculated radial gradient (slope of solid lines in Fig. 2) for each of the three energy intervals. In the lowest energy interval (7.1-10.6 MeV/nuc) the spectrum of anomalous O is changing with time [*Cummings et al.*, 1985], which may contribute to the observed variation in the radial gradient. Above 10.6 MeV/nuc no such energy spectral changes are found and the resulting gradient is remarkably constant. In the 10.6-17.1 MeV/nuc interval the average value of the gradient is 10.7 ± 0.6%/AU, somewhat lower than the 15 ± 3%/AU found by

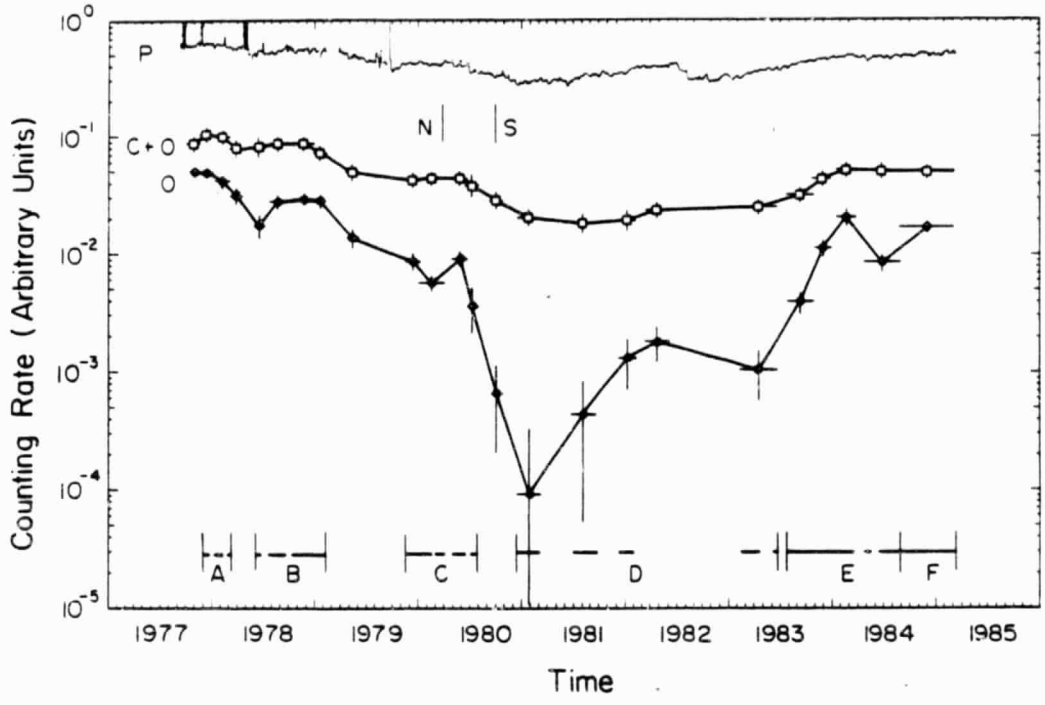

Fig. 1. Counting rates of three particle types from Voyager 1 telescopes. P labels the penetrating rate from the high-energy telescope (mainly protons >75 MeV), C+O labels the rate of 40-106 C+O, and O labels the rate of 5.6-17.2 MeV/nuc anomalous oxygen. The approximate times of the solar magnetic field reversal in the northern (N) and southern (S) polar regions are indicated by the vertical bars [*Webb et al.*, 1984]. The horizontal bars represent quiet-time intervals as discussed in the text.

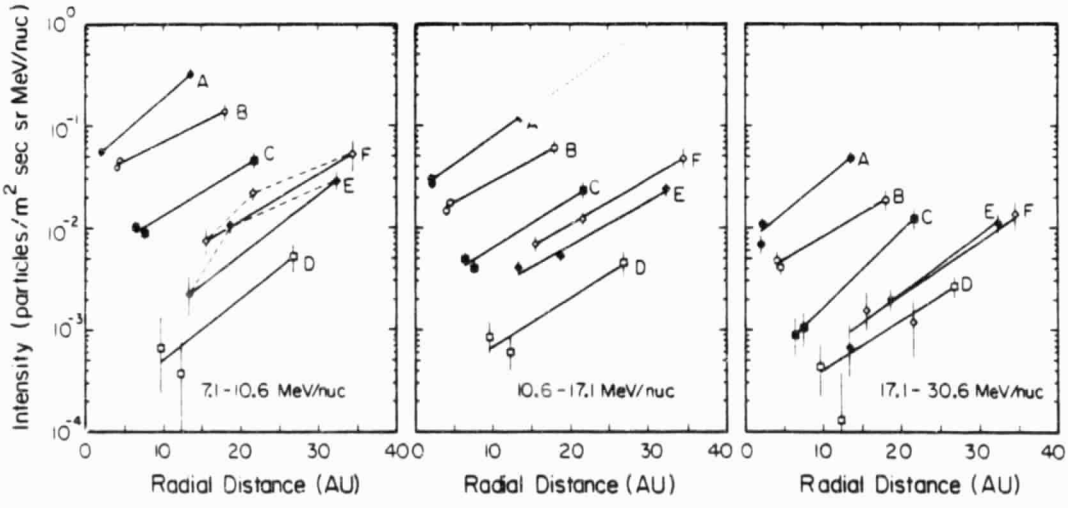

Fig. 2. Intensity of anomalous O versus heliocentric radial distance in three energy intervals from the V1, V2, and P10 cosmic-ray instruments. The labels A-F refer to the six quiet-time intervals chosen for analysis. The lines are described in the text.

Webber et al. [1981] for the period 1972-79. It is clear from Figs. 2 and 3 that the radial gradient for all three energy intervals has not changed appreciably with time or radial distance, maintaining a value between ~10-15%/AU despite the fact that the intensity has varied by more than a factor of 100.

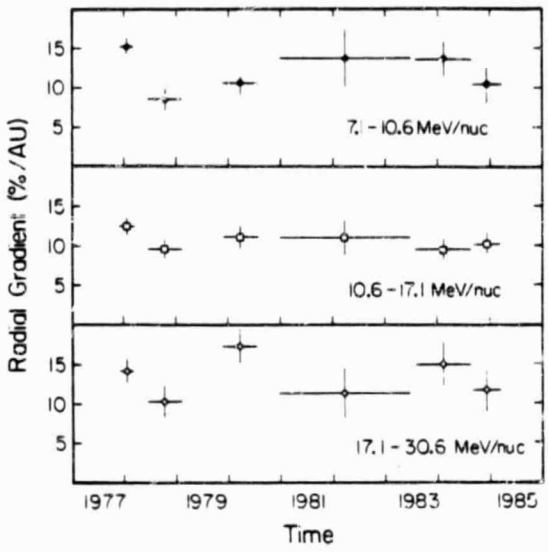

Fig. 3. Measured radial gradients of anomalous O versus time for the three energy intervals of Fig. 2.

3. **Discussion.** We believe that the constancy of the gradient with respect to time both before and after the solar magnetic field reversal in 1980, and during a period when the intensity change was a factor ~100 is an important clue and constraint on the solar modulation process. In conventional modulation theory, if the effects of particle streaming in the interplanetary medium can be neglected, then the radial gradient, G_r, and the radial diffusion coefficient, κ_r, are related by $G_r = CV/\kappa_r$. The average solar wind velocity, V, and κ_r change only slightly over a solar cycle (see *Hedgecock* [1974] and *Feldman et al.* [1979]). Also the Compton-Getting coefficient C, which is related to the spectral shape, does not change appreciably since the spectral shape remains similar above ~10 MeV/nuc. Thus, if the gradient can be described by these local parameters, it would be expected to be constant as observed.

In this simple conventional modulation model in which κ_r is independent of radial distance r, the particle intensity j at r is given by $j = j_b \exp[CV(r-r_b)/\kappa_r]$, where j_b is the intensity at the modulation boundary. Since C, V, and κ_r are not changing appreciably with time, and assuming j_b is constant, the large modulation at a given position would require a time variation in the boundary location r_b. The magnitude of the required change in the boundary distance can be estimated from Fig. 2b. The dotted line is an extrapolation of the intensity in the 10.6-17.1 MeV/nuc energy range during the time of solar minimum to the position of P10 (27 AU) during the solar maximum period of interval D. The implied intensity change from period A to D at 27 AU is a factor of 136 ± 52, indicating that most of the modulation during period D is occurring beyond 27 AU. Using the average radial gradient for this energy interval we find that the required change in the boundary distance r_b is 46 ± 4 AU. A similar boundary shift has been suggested by *Evenson et al.* [1979] to explain electron observations.

Such a boundary shift would also produce changes in the intensity of other particle species. For example, the penetrating particle rate (P) in Fig. 1 shows a variation from solar minimum to solar maximum of a factor ~2. The median rigidity of the particles dominating this rate is ~1.8 GV, the same rigidity as 7 MeV/nuc anomalous O if O is singly charged (as expected if they are freshly-ionized neutrals [*Fisk et al.*, 1974]). The spectral shapes of the anomalous O (above 10 MeV/nuc) and high-energy protons are similar (spectral index ~-2) implying they have similar values of C. Since $\kappa_r \propto \beta f(R)$, where β is the particle velocity and R is the rigidity, the expected gradient for the P rate can be scaled from the gradient of anomalous O by $G_r(P) = G_r(O)(\beta_O/\beta_P) \sim 10(.12/.89) = 1.5\%$/AU, a value in approximate agreement with observations by others (see *McKibben et al.* [1982] and *Lockwood and Webber* [1984]). The intensities at two different times are related by $j_1/j_2 = \exp(G_r(\delta r_b))$. Therefore, a boundary change of 46 AU and a radial gradient of 1.5-3%/AU would result in $j_1/j_2 = 2$-4 for the penetrating particles, similar to what we observe.

An alternative way to accomplish the same modulation without changing the boundary distance is to decrease κ_r, and thus increase the gradient, in a localized shell of turbulence in the outer heliosphere, as suggested by *Burlaga et al.* [1984]. The observed change in modulation

would require, for example, an increase in the anomalous O gradient from 11%/AU to 44%/AU in a shell 15AU thick.

It is also possible that variations in the source of the anomalous O may contribute to the observed solar cycle variation. We note that *Jokipii* [1985], using a model of the anomalous component in which the particles are accelerated at the polar termination shock and drift to the solar equatorial regions, has calculated spectra of anomalous O that depend on the polarity of the magnetic field and which are in reasonable agreement with observations of changes in the spectra associated with the magnetic field reversal (see *Cummings et al.* [1985]). However, we find no evidence of a change in the gradient of the anomalous O at the time of the solar magnetic field reversal as would presumably be expected from such a model.

4. Acknowledgments. We are grateful to R. E. Vogt and other CRS team members consisting of scientists and engineers at the California Institute of Technology, the Goddard Space Flight Center, the University of Arizona, and the University of New Hampshire. This work was supported in part by NASA under contract NAS 7-918 and grant NGR 05-002-160.

5. References.

Burlaga, L. F., F. B. McDonald, N. F. Ness, R. Schwenn, A. J. Lazarus, and F. Mariani, *J. Geophys. Res., 89*, 6579, 1984.

Cummings, A. C., E. C. Stone, and W. R. Webber, *Ap. J. (Letters), 287*, L99, 1984.

Cummings, A. C., E. C. Stone, and W. R. Webber, *19th Internat. Cosmic-Ray Conf., La Jolla*, paper SH4.6-1, 1985.

Evenson, P., J. Caldwell, S. Jordan, and P. Meyer, *J. Geophys. Res., 84*, 5361, 1979.

Feldman, W. C., J. R. Asbridge, S. J. Bame, and J. T. Gosling, *J. Geophys. Res., 84*, 7371, 1979.

Fisk, L. A., B. Kozlovsky, and R. Ramaty, *Ap. J. (Letters), 190*, L35, 1974.

Hedgecock, P. C., *J. Geophys. Res., 79*, 4775, 1974.

Jokipii, J. R., submitted to *J. Geophys. Res.*, 1985.

Lockwood, J. A., and W. R. Webber, *Ap. J., 279*, 151, 1984.

McKibben, R. B., K. R. Pyle, and J. A. Simpson, *Ap. J. (Letters), 254*, L23, 1982.

McDonald, F. B., N. Lal, J. H. Trainor, M. A. I. Van Hollebeke, and W. R. Webber, *Ap. J., 216*, 9[illegible] 1977.

Stone, E. C., R. E. Vogt, F. B. McDonald, B. J. Teegarden, J. H. Trainor, J. R. Jokipii, and W. R. Webber, *Space Sci. Rev., 21*, 355, 1977.

Webb, D. F., J. M. Davis, and P. S. McIntosh, *Solar Phys., 92*, 109, 1984.

Webber, W. R., F. B. McDonald, T. T. Von Rosenvinge, and R. A. Mewaldt, *17th Internat. Cosmic-Ray Conf., Paris, 10*, 92, 1981.

D-15

Solar Modulation and Interplanetary Gradients of the Galactic Electron Flux 1977-1984

S. P. Christon, A. C. Cummings, and E. C. Stone

California Institute of Technology, Pasadena, CA 91125 USA

W. R. Webber

University of New Hampshire, Durham, NH 03824 USA

Previously, only one measurement of electrons at a location remote from earth has been reported [*Eraker*, 1982]. That measurement was made with a cosmic ray instrument on board the Pioneer 10 spacecraft during the period from 1972 - 1980, when Pioneer proceeded outward from 1 to 21.5 AU. Electrons of 1.75 - 25 MeV were observed. This energy range appears to be dominated by Jovian electrons, and no significant temporal or radial effects due to galactic electrons were observed.

In this paper we report on the flux of electrons with energy from ~ 10 - 180 MeV measured with the electron telescope on the Voyager 1 and 2 spacecraft [*Stone et al.*, 1977] in the heliocentric radial range 1 - 22 AU between 1977 and 1984. Jovian electrons were clearly observable between 1978 and 1983 (radial range 2 - 12 AU) at energies below ~ 50 MeV [*Christon et al.*, 1985]. Above ~ 50 MeV the electron intensity exhibited temporal variations generally related to the 11 year modulation of protons > 75 MeV. The overall magnitude of the electron intensity changes between the maximum intensity observed in 1977 and the minimum intensity in 1981 was a factor ~ 2, also comparable to that observed for > 75 MeV protons. By early 1985 the electron intensity had apparently recovered to the level observed in 1977 whereas the proton intensity was still about 20% lower. A detailed interpretation of these electron variations in all energy channels depends on an accurate subtraction of background induced by energetic protons of a few 100 MeV. This subtraction is facilitated by calibration results at several energies. Further results on these temporal variations and limits on possible interplanetary gradients will be reported.

This work was supported in part by NASA under contract NAS 7-918 and grant NGR 05-002-160.

References.

Christon, S. P., A. C. Cummings, E. C. Stone, and W. R. Webber, *19th Internat. Cosmic-Ray Conf., La Jolla*, paper SH1.5-18, 1985.

Eraker, J. H., *Ap. J., 257*, 862, 1982.

Stone, E. C., R. E. Vogt, F. B. McDonald, B. J. Teegarden, J. H. Trainor, J. R. Jokipii, and W. R. Webber, *Space Sci. Rev., 21*, 355, 1977.